



HAL
open science

Contributions of Internal Variability and External Forcing to the Recent Trends in the Southeastern Pacific and Peru-Chile Upwelling System

Beyrem Jebri, Myriam Khodri, Vincent Echevin, Guillaume Gastineau, Sylvie Thiria, Jérôme Vialard, Nicolas Lebas

► **To cite this version:**

Beyrem Jebri, Myriam Khodri, Vincent Echevin, Guillaume Gastineau, Sylvie Thiria, et al.. Contributions of Internal Variability and External Forcing to the Recent Trends in the Southeastern Pacific and Peru-Chile Upwelling System. *Journal of Climate*, 2020, 33 (24), pp.10555-10578. 10.1175/JCLI-D-19-0304.1 . hal-03155768

HAL Id: hal-03155768

<https://hal.sorbonne-universite.fr/hal-03155768v1>

Submitted on 2 Mar 2021

HAL is a multi-disciplinary open access archive for the deposit and dissemination of scientific research documents, whether they are published or not. The documents may come from teaching and research institutions in France or abroad, or from public or private research centers.

L'archive ouverte pluridisciplinaire **HAL**, est destinée au dépôt et à la diffusion de documents scientifiques de niveau recherche, publiés ou non, émanant des établissements d'enseignement et de recherche français ou étrangers, des laboratoires publics ou privés.

Contributions of Internal Variability and External Forcing to the Recent Trends in the Southeastern Pacific and Peru–Chile Upwelling System

BEYREM JEBRI, MYRIAM KHODRI, VINCENT ECHEVIN, GUILLAUME GASTINEAU, SYLVIE THIRIA, JÉRÔME VIALARD, AND NICOLAS LEBAS

LOCEAN-IPSL, Sorbonne-Université, CNRS/IRD/UPMC/MNHN, Paris, France

(Manuscript received 25 April 2019, in final form 30 December 2019)

ABSTRACT


In a warming world context, sea surface temperature (SST) off central-south Peru, northern Chile, and farther offshore increases at a slower rate than the global average since several decades (i.e., cools, relative to the global average). This tendency is synchronous with an interdecadal Pacific oscillation (IPO) negative trend since ~1980, which has a cooling signature in the southeastern Pacific. Here, we use a large ensemble of historical coupled model simulations to investigate the relative roles of internal variability (and in particular the IPO) and external forcing in driving this relative regional cooling, and the associated mechanisms. The ensemble mean reproduces the relative cooling, in response to an externally forced southerly wind anomaly, which strengthens the upwelling off Chile in recent decades. This southerly wind anomaly results from the poleward expansion of the Southern Hemisphere Hadley cell. Attribution experiments reveal that this poleward expansion and the resulting enhanced upwelling mostly occur in response to increasing greenhouse gases and stratospheric ozone depletion since ~1980. An oceanic heat budget confirms that the wind-forced upwelling enhancement dominates the relative cooling near the coast. In contrast, a wind-forced deepening of the mixed layer drives the offshore cooling. While internal variability contributes to the spread of tendencies, the ensemble-mean relative cooling in the southeastern Pacific is consistent with observations and occurs irrespectively of the IPO phase, hence, indicating the preeminent role of external forcing.

1. Introduction

The Humboldt Peru–Chile upwelling system (PCUS; Strub et al. 1998) is one of the most productive oceanic regions globally in terms of phytoplankton (Chavez et al. 2008; Kämpf and Chapman 2016) and represents one of the leading fisheries in the world, thriving with high biological diversity (Cushing 1971; Fréon et al. 2009). As in other eastern boundary upwelling systems, alongshore equatorward wind stress and the associated wind stress curl drive coastal upwelling. The action of the surface wind stress pushes surface waters offshore and pumps up deeper, cold, and nutrient-rich waters (Sverdrup 1938), triggering the high surface productivity. Ecosystems and fisheries are already under strong pressure from climate change globally, with projections pointing to an overall oceanic warming, acidification,

deoxygenation, and reduced primary productivity (e.g., Bopp et al. 2013, Beaugrand et al. 2019). Due to the strong socioeconomic relevance of the PCUS (Ibarra et al. 2000; Pérez et al. 2010), it is critical to further investigate and quantify the potential impacts of climate change in this region.

Previous works documenting the PCUS long-term upwelling trends have mostly relied on wind stress based upwelling indices over recent decades (e.g., Aravena et al. 2014) or estimates from phase 5 of the Coupled Model Intercomparison Project (CMIP5) global circulation models to infer wind-driven upwelling intensity variations into the twenty-first century (e.g., Rykaczewski et al. 2015; Wang et al. 2015). Analyses from general circulation models have suggested mixed results and even contradictory trends for the Humboldt system (Oyarzún and Brierley 2019). On the other hand, sea surface temperature (SST) cooling trends (Figs. 1a,b) have been observed off Chile since the 1980s (Falvey and Garreaud 2009) and off central-south Peru since the 1950s (Gutiérrez et al. 2011). These coastal trends have been interpreted as an indirect evidence of wind-driven upwelling intensification.

 Denotes content that is immediately available upon publication as open access.

Corresponding author: Beyrem Jebri, beyrem.jebri@locean-ipsl.upmc.fr

DOI: 10.1175/JCLI-D-19-0304.1

© 2020 American Meteorological Society. For information regarding reuse of this content and general copyright information, consult the AMS Copyright Policy (www.ametsoc.org/PUBSReuseLicenses).

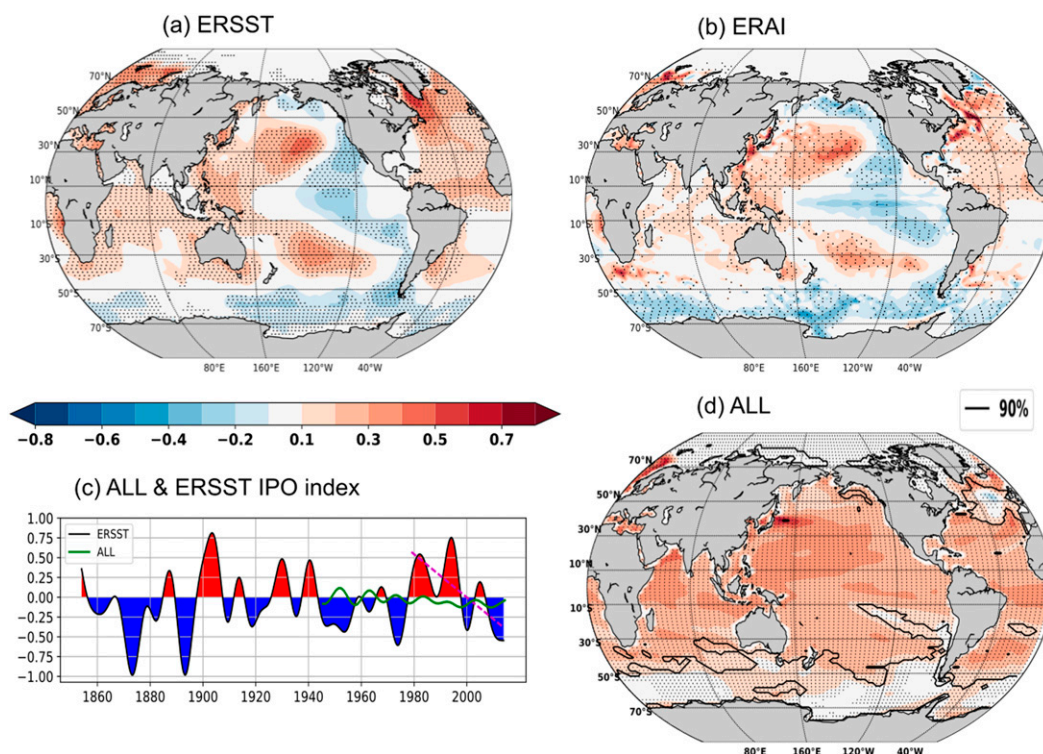


FIG. 1. Sea surface temperature trend in austral summer (December–February) for the period 1980–2014, in $^{\circ}\text{C decade}^{-1}$ for (a) ERSSTv4, (b) ERA-Interim, and (d) ALL ensemble mean. Stippling denotes regions where the observed or ensemble mean trend is significant at the 90% confidence level. The black contour lines in (d) indicate where at least 90% of the ALL ensemble members have a positive sea surface temperature trend. (c) IPO TPI index from ERSSTv4 dataset. The green curve shows the ALL ensemble-mean IPO index. The purple dashed line corresponds to the 1980–2014 IPO index linear trend from ERSSTv4.

Low-frequency SST changes in this region can also be associated with internal climate variability (Montecinos et al. 2003; Vargas et al. 2007). While El Niño–Southern Oscillation (ENSO; e.g., McPhaden et al. 2006) is the leading mode of interannual climate variability in the Pacific Ocean, its decadal fluctuations imprint a pan-Pacific pattern of coherent SST decadal variability (Newman et al. 2016) through atmospheric teleconnections (e.g., Alexander et al. 2002). This pattern is known as the interdecadal Pacific oscillation (IPO), and is the leading mode of internal, decadal to multidecadal variability in the Pacific Ocean (Folland et al. 1999; Power et al. 1999). The IPO SST pattern is broadly similar to that of ENSO, but less equatorially confined in the eastern Pacific and more prominent in the extratropical latitudes (Minobe 1997; Minobe 1999; Deser et al. 2004; Deser et al. 2010). The IPO has experienced a trend from a positive (i.e., El Niño-like) to a negative (La Niña-like) phase over the 1980–2014 period (Fig. 1c), associated with an intensification of Pacific trade winds and with a shoaling of the thermocline in the eastern equatorial Pacific (e.g., Balsameda et al. 2013; de Boissésou et al. 2014; England

et al. 2014; Kociuba and Power 2015; Choi et al. 2016; Gastineau et al. 2018). Poleward propagating coastal waves and a shoaling of the nearshore thermocline may also play a key role in modulating SST at decadal time scales off Chile (e.g., Montecinos et al. 2007). Such an IPO phase transition during the 1980–2014 period is indeed associated with a central and eastern equatorial Pacific cooling that extends toward midlatitudes and in particular into the southeastern Pacific (hereafter, SEP) and the broad PCUS region (Figs. 1a,b). Thus, the IPO might have contributed to the recent cooling trend in this region.

Nevertheless, the PCUS trends over recent decades could also result from external forcing. Under greenhouse gas forcing continental surface temperatures increase more than nearby SSTs because of the drier environment and larger lapse-rate over land (e.g., Joshi et al. 2008; Dommenges 2009). This lowers pressure over land (e.g., Bayr and Dommenges 2013) and potentially strengthens the land–sea sea level pressure gradient and the upwelling-favorable alongshore wind stress (Bakun et al. 2010). Indeed, CMIP5 model projections point to a

significant increase in the duration and intensity of upwelling-favorable winds in the poleward portions of the four major eastern boundary upwellings (California, Canary, Humboldt, Benguela), which highly correlates to the land–sea temperature gradient (Wang et al. 2015).

The alongshore winds intensification is, however, not accompanied by a clear reinforcement of the land low pressure system either in CMIP5 historical simulations or in projections (Ryckaczewski et al. 2015). Belmadani et al. (2014) suggest that the enhancement of upwelling-favorable winds over the PCUS are rather due to subtropical southerly wind anomalies linked to a poleward expansion of the Southern Hemisphere Hadley cell (HC). Several observational datasets and reanalyses indeed show that the Southern Hemisphere HC southern edge ($\sim 20^{\circ}\text{S}$ in the current climate) has shifted southward by about 0.3° – 0.5° of latitude per decade since 1979 (Johanson and Fu 2009; Hu et al. 2011, 2013; Choi et al. 2014; Staten et al. 2018; Grise et al. 2019), with the largest poleward expansion during austral summer (Chen et al. 2014). Climate model experiments suggest that the HC poleward expansion is forced by the ozone depletion from 1979 to the late 1990s (e.g., Son et al. 2010; McLandress et al. 2011; Hu et al. 2013; Min and Son 2013) and by the rising concentration of atmospheric greenhouse gases (Lu et al. 2007; Staten et al. 2012; Quan et al. 2014; Adam et al. 2014). However, the tendency toward more La Niñas in relation with the recent IPO trend may also contribute to the HC poleward shift (Nguyen et al. 2013).

To our knowledge, previous studies have not specifically examined (i) the respective role of anthropogenic forcing and internal climate variability in long-term trends in the PCUS, (ii) the specific role of the HC expansion on PCUS changes and its attribution to specific sources of external forcing, and (iii) the physical processes responsible for the weak SST warming in the southeastern Pacific (relative to the global mean) over the last decades. These are the questions addressed in this study. Here, we assess the 1940–2020 PCUS climate changes, using observations and a set of 20–30-member ensembles conducted with the IPSL-CM5A-LR (Dufresne et al. 2013) coupled general circulation model. The paper is organized as follows: in section 2, we describe the model, data, and methods. Section 3 presents the globally averaged SST trends in the model, and then focuses on the PCUS region, for a validation of the ensemble-mean climatology and overview of the ensemble trends. In section 4, we explore the relative roles of externally forced versus internal variability. Section 5 describes the contribution of various external forcing (greenhouse gases, stratospheric ozone, volcanoes) on the Hadley cell expansion and PCUS.

In section 6, we investigate the mechanisms responsible for the relative SST cooling in the southeastern Pacific. Results are discussed in section 7 before concluding.

2. Methods and data

a. The coupled model

We used the CMIP5 version of the Institut Pierre-Simon Laplace (IPSL) atmosphere–ocean general circulation model, called IPSL-CM5A-LR (Dufresne et al. 2013). LR stands for low resolution, as the atmospheric grid resolution is 1.87° in latitude and 3.75° in longitude. It includes the LMDZ5A atmospheric component (Hourdin et al. 2013), with 39 hybrid sigma-pressure levels, including 15 in the stratosphere. LMDZ5A is coupled to the ORCHIDEE (Krinner et al. 2005) land surface component. The oceanic component uses Nucleus for European Modelling of the Ocean (NEMO), version 3.2 (Madec 2008), with 31 vertical levels (and resolution decreasing from 10 m near the surface to 500 m toward the bottom), a mean spatial horizontal resolution of about 2° (with a refinement to a 0.5° latitudinal resolution near the equator). The ocean model includes the LIM2 sea ice model (Fichefet and Maqueda 1997).

Compared to other CMIP5 models, IPSL-CM5A-LR has a relatively large transient climate response, reaching 2 K per CO_2 doubling. It thus ranks among the high-sensitivity climate models of CMIP5 (multimodel mean of 1.82 ± 0.63 K) (Andrews et al. 2012; Forster et al. 2013), due to a large positive low-level clouds feedback (Brient and Bony 2013). Previous works show that this model reproduces ENSO variability with two spectral peaks around 3–3.5 years and beyond 4 years, which is in good qualitative agreement with observations (Bellenger et al. 2014). IPSL-CM5A-LR is also realistic for other aspects of the climate variability. It simulates well the characteristics of observed North Pacific variability (Fleming and Anchukaitis 2016) and the links between ENSO and the IPO (Nidheesh et al. 2017). However, like many global climate models, IPSL-CM5A-LR simulates a double intertropical convergence zone (ITCZ) and the classical cold tongue bias in the Pacific (Dufresne et al. 2013). The observed ENSO seasonal phase locking is also not well captured (Bellenger et al. 2014). Last, IPSL-CM5A-LR also has a rather strong cold bias for the surface air temperature, in particular in the midlatitudes.

b. Experimental protocol

We performed four IPSL-CM5A-LR ensembles with historical external forcing for the 1940–2020 period (see Table 1). The first ensemble of 30 members (referred to as the ALL ensemble) uses the historical CMIP5

TABLE 1. Ensemble size and external forcing considered over the 1940–2020 period for the ensemble IPSL-CM5A-LR experiments used in this study (see section 2b).

Experiment name	Used external forcing			Model members
	Greenhouse gases	Ozone	Volcanic forcing	
ALL	×	×	×	30
GHG	×	—	—	20
OZ	—	×	—	20
VOLC	—	—	×	20

(Taylor et al. 2012) concentrations of greenhouse gases (GHG) from 1940 to 2005 and from RCP8.5 between 2006 and 2020 (Riahi et al. 2011). The standard CMIP5 ozone concentration used in IPSL-CM5A-LR was calculated from a separate atmospheric simulation with interactive atmospheric chemistry (Szopa et al. 2013). We also use the historical stratospheric aerosol forcing from the main volcanic eruptions by prescribing the aerosol optical depth, as given in Sato et al. (1993) (2012 updated version).

Three other ensembles use each forcing individually, namely either volcanic (referred to as VOLC), greenhouse gases (referred to as GHG), or ozone (referred to as OZ) forcing, while maintaining other forcing at their 1940 level. The VOLC, GHG, and OZ ensembles have 20 members each. Each ensemble member starts in January 1940 from randomly sampled initial conditions (31 December) chosen over 1920–60 in a set of IPSL-CM5A CMIP5 historical simulations (initiated in 1870) using all forcings (i.e., similar to ALL). Tropospheric aerosols forcing is maintained to the preindustrial level in all simulations.

Taking initial conditions that sample random phases of the internal climate variability guarantees that this variability is largely uncorrelated across members from the start of the experiments. The ensemble averaging of the large number of members hence damps the internal climate variability by a factor of \sqrt{n} in a n -member ensemble, so that it is reduced by a factor of ~ 5.5 and 4.5 in the 30- and 20-member ensembles, respectively. It allows effective isolation of the externally forced variability. This is demonstrated in Fig. 1c, which shows the ALL ensemble mean IPO index (green curve) whose variability is much smaller than the observed one, confirming that the large ensemble averaging successfully damps out internal variability.

c. Trend analysis and statistical testing

All anomalies are calculated by removing the 1941–61 monthly mean seasonal cycle to the time series. We then applied a Hanning filter with a 7-yr cutoff period to

focus only on the decadal variability. All the linear trends in the paper are computed from the low-pass-filtered time series, using least squares. On time series plots, the ensemble mean is plotted, along with an estimate of the intermember spread. Depending on the figure, this spread is either estimated from the 5th and 95th percentiles or from the 90% confidence interval, assuming Gaussian distributions and considering each member as independent. Trend maps are computed over 1980–2014 and regions where the trend (ensemble mean trend for simulations) is significantly different from zero at 90% confidence level are estimated with a Wald test using a t distribution for the test statistic. We also indicate regions where more than 60% and 90% of the members display anomalies of the same sign as the ensemble mean trend.

d. Upwelling and IPO indices

We considered four main variables to characterize the variations of the PCUS in each ensemble: meridional surface wind stress (τ_y), wind stress curl (ζ), SST, and vertical velocity at 100-m depth (w_{100}). Because the regions over which the variability of these variables is homogenous are not necessarily square boxes, and may depend on the variable, we have defined specific regions for each variable according to their covariability. We defined regions in the broad southeast Pacific region (10°N–52°S, 113°–66°W) by clustering, for each variable, nearby grid points with similar temporal variations based on correlations of their 1940–2020 time series. To do so we combined the ClustVar (Vigneau and Qannari 2003) algorithms and the self-organizing map (SOM) (Kohonen 1998) topological ordering properties in order to aggregate variables together according to their covariability. We then extract spatial regions of coherent temporal variability from this clustering. To analyze the IPO, we use the SST tripole index (TPI; Henley et al. 2015), defined as the central equatorial Pacific SST (10°S–10°N, 170°E–90°W) minus the average of northwest (25°–45°N, 140°E–145°W) and southwest (15°–50°S, 150°E–160°W) Pacific SST, smoothed using a 13-yr Chebyshev low-pass filter.

e. Mixed layer heat budget

We compute a simplified mixed layer heat budget for each member of the ALL ensemble using monthly data, in order to quantify the respective contributions of surface heat flux and oceanic processes to the SST tendencies. The mixed layer heat budget is expressed as follows:

$$\Delta \text{SST}(t) = \int_{t_0}^t \left[\frac{Q_{\text{atm}}(t')}{\rho \times c_p \times h(t')} \right] dt' + \text{OCE}_{\text{dyn}}(t), \quad (1)$$

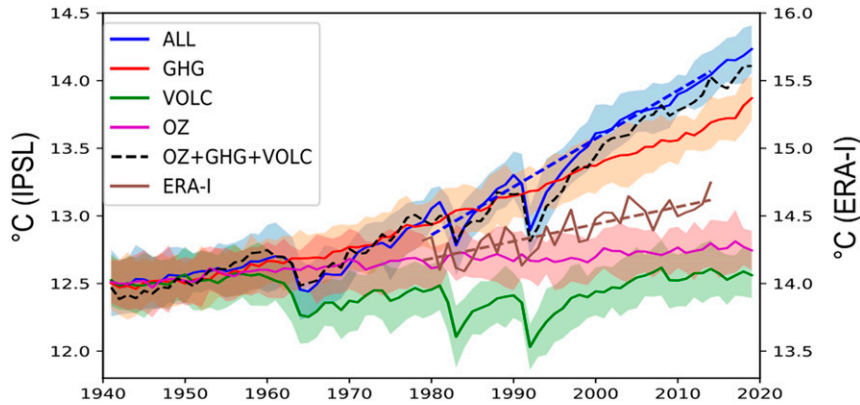


FIG. 2. Global annual mean 2-m temperature, in $^{\circ}\text{C}$, for ALL (blue), GHG (red), VOLC (green), OZ (purple), and ERA-Interim (brown). The sum of corresponding anomalies from GHG, VOLC, and OZ is shown as a black dashed curve; note that the left y axis for the ensemble simulations is offset by 1.5°C as compared to the right y axis for ERA-I. Thick solid lines indicate the ensemble means; shading shows the spread corresponding to 90% of the members according to a t distribution. Dashed blue and brown lines show the 1980–2014 linear trends.

with

$$Q_{\text{atm}} = Q_{\text{lw}} + Q_{\text{flat}} + Q_{\text{sens}} + Q_{\text{sw}} - Q_{\text{swh}}, \quad (2)$$

where $\Delta\text{SST}(t)$ is the SST monthly variation between t_0 (taken as 1950) and t . The first term of the right-hand side in Eq. (1) represents the SST anomaly due to surface heat flux. The $Q_{\text{atm}}(t)$ represents the anomalous net surface heat flux into the oceanic mixed layer. The $h(t)$ is the thickness of the mixed layer defined as the depth at which the vertical eddy diffusivity coefficient falls below a given value (here taken equal to background value of $5\text{ cm}^2\text{ s}^{-1}$) and can be interpreted as a maximum penetration depth of the turbulent motion in the surface layer. Here C_p and ρ denote the seawater specific heat ($4000\text{ J kg}^{-1}\text{ K}^{-1}$) and a reference density (1025 kg m^{-3}), respectively. We compute the first term on the right-hand side of the equation using monthly mean averages. The net surface heat flux is composed of Q_{sw} the shortwave radiative flux at the ocean surface, Q_{swh} the shortwave radiative flux transmitted through the bottom of the mixed layer, Q_{lw} the long-wave radiative flux, Q_{flat} the latent heat flux, and Q_{sens} the sensible heat flux. The net heat flux is defined positive downward. The second term on the right-hand side of Eq. (1) is the SST anomaly due to ocean dynamics $\text{OCE}_{\text{dyn}}(t)$ (including the local influence of upwelling) estimated as a residual. It corresponds to ocean processes such as the horizontal and vertical advection of temperature and horizontal and vertical turbulent mixing. Since the ocean dynamical term is estimated as a residue from the SST change and the atmospheric heat flux effect, it may also contain errors associated with neglecting the submonthly variations

of surface heat flux and mixed layer depth when computing the atmospheric forcing term.

f. Observations and reanalyses

Our study uses global gridded monthly analyses of NOAA Optimal Interpolation Sea Surface Temperature, version 2 (OISSTv2; Reynolds et al. 2002), which begins in December 1981 and ERSSTv4 (Huang et al. 2015), which starts in 1854. We also analyze the SST seasonal cycle and the wind stress patterns from SODA2.2.1 Ocean Reanalyses climatology (Carton and Giese 2008), representative of the 1941–61 period. Last, we use sea level pressure (SLP), surface wind stress, 2-m air temperature, 3D wind, and pressure fields (to compute the atmospheric meridional overturning streamfunction) from the European Centre for Medium-Range Weather Forecasts (ECMWF) ERA-Interim reanalysis (ERA-I) over 1979–2014 (Dee et al. 2011), twentieth-century NOAA-CIRES (NOAA-20C; Compo et al. 2011), and NCEP (Kalnay et al. 1996).

3. Model validation

a. Global warming signal and contributions from individual forcing sources

Figure 2 displays the global annual mean 2-m air temperature time series, in ALL, VOLC, GHG, OZ, and ERA-I. The ALL simulation, which includes all sources of forcing, significantly overestimates the observed global heating rate since ~ 1980 . This is mainly due to two factors. As noted in the introduction, the tropospheric aerosol change and the cooling effects associated to sulfate aerosols (e.g., Boer et al. 2000;

Allen and Ajoku 2016) are omitted in these simulations (see section 2b). The overestimated warming also originates from the large climate sensitivity of IPSL-CM5A-LR (Forster et al. 2013). Besides, the (GHG + VOLC + OZ) mean 2-m air temperature fits well that of ALL, suggesting linear additivity of the response to individual external forcing, in terms of global mean 2-m air temperature anomalies. GHG forcing is clearly the main driver of the 2-m air temperature increase and explains most (+0.75°C) of the 1980–2014 warming trend in ALL (+0.99°C), consistent with the behavior of other CMIP5 models (Knutson et al. 2017). Only a weak warming (+0.18°C) is simulated in OZ over the period. This probably reflects the transient adjustment of the climate system toward a warmer state. It could also be due to the small increase in tropospheric ozone acting as a greenhouse gas. VOLC illustrates the strong cooling contribution to ALL a few years following the three main historical volcanic eruptions, namely Agung in 1963, El Chichón in 1982, and Pinatubo in 1991. We further use the GHG, VOLC, and OZ experiments in section 5c to attribute changes in the PCUS to specific forcing sources.

b. Global warming trend pattern

The comparison of the ALL ensemble-mean and observed 1980–2014 SST trends reveals large differences (Figs. 1a,b,d). The two observational products display significant positive SST trends over the North Atlantic Ocean, most of the western Indian Ocean, the tropical and subtropical western Pacific, while weak cooling trends are observed over much of the eastern equatorial Pacific. The observed SST trends capture the negative IPO-like trend pattern (Figs. 1a,b; Deser et al. 2010), with coastal cooling off California and Chile–Peru (Falvey and Garreaud 2009; Gutiérrez et al. 2011) and over most of the equatorial Pacific. The ensemble averaging in ALL filters out internal variability such as that of the IPO, hence reveals the externally forced warming over the period. As a result, the ALL experiment (Fig. 1d) features a large-scale positive trend, largest in subtropical latitudes (Foster and Rahmstorf 2011). The lack of tropospheric aerosol forcing and overestimated climate sensitivity also probably contribute to the more preeminent warming than in observations. Despite these differences, the ALL ensemble mean reveals a weak warming trend over much of the SEP, the Southern Ocean and the subpolar Atlantic, consistently with the SST patterns simulated by most models in response to natural and anthropogenic forcing of the twentieth century (e.g., Stouffer et al. 1989). In particular, no significant SST trend is simulated off the coasts of central and south Chile (30°–50°S). This weak surface warming off Chile can be

interpreted as an indirect evidence of the intensification of upwelling in the PCUS in response to the anthropogenic forcing, as suggested by Belmadani et al. (2014), Wang et al. (2015), and Rykaczewski et al. (2015).

c. Peru–Chile upwelling system

In this subsection, we validate the climatological structure of the PCUS in the ALL experiment. Coastal upwelling dynamics are very sensitive to the wind stress structure near the coast (Capet et al. 2004; Small et al. 2015; Renault et al. 2016). Alongshore wind stress at the coast drives the offshore Ekman transport that leads to coastal upwelling. The wind stress also weakens when approaching the coast due to the enhanced friction on land, generating negative wind stress curl and upward Ekman pumping (e.g., Belmadani et al. 2014). Despite its coarse resolution, the model reproduces the first-order seasonal characteristics of the PCUS, namely the intensification of meridional wind stress, associated coastal cooling and positive oceanic velocities off Chile (~20°–30°S) in boreal winter (DJF) and off south Peru (~15°–20°S) in boreal summer (JJA) (Fig. 3). The known “cold tongue” bias of coupled climate models (e.g., Li and Xie 2014) is visible in JJA, but does not extend into the PCUS.

d. Hadley circulation

We here diagnose the Hadley circulation in our model based on the meridional streamfunction. The meridional streamfunction in ALL (Figs. 4a,b, black contours) is consistent with results from previous model studies (Gastineau et al. 2008; Kim et al. 2017) and reanalyses (Mitas and Clement 2005). We define the Southern Hemisphere Hadley cell edge as the linearly interpolated latitude for which the 500-hPa meridional streamfunction (ψ_{500}) is equal to zero. There is an overall good agreement between the ALL and ERA-I ψ_{500} (Fig. 4c) despite a southern edge located too much equatorward (2.2° latitude in DJF and 0.9° in JJA) as in other coupled general circulation models. This discrepancy is linked to the positions of subtropical jets that are also positioned too close to the equator (Barnes and Polvani 2013; Arakelian and Codron 2012).

4. Long-term regional trends and external forcing contribution

a. Regional trends in the Peru–Chile upwelling system

We already underlined that the broad SEP region warms less than the global average in the previous section. To visualize that signal more clearly, and to get rid of the overestimated warming in our simulations, we now examine SST trends relative to the global average

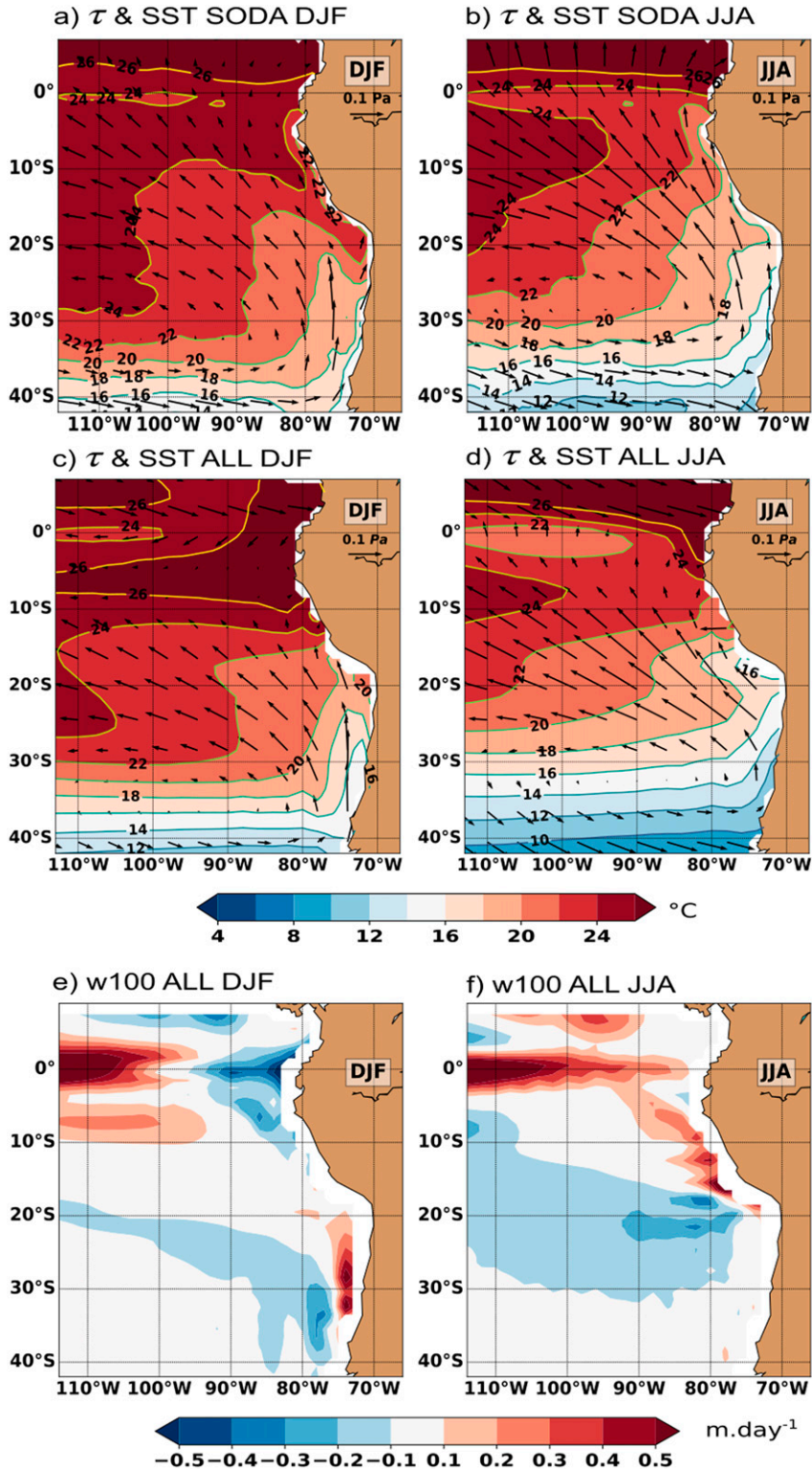


FIG. 3. Mean climatological sea surface temperature (SST, in °C) and surface wind stress (τ , in Pa) for the 1941–61 period for (a),(b) SODA2.2.4 and (c),(d) ALL ensemble mean, in December–February (DJF) and June–August (JJA), respectively. (e),(f) Mean climatological ocean vertical velocity at 100-m depth (W100, m day⁻¹) over the 1941–61 period for ALL ensemble mean in DJF and JJA. Red (blue) shading corresponds to upward (downward) velocity.

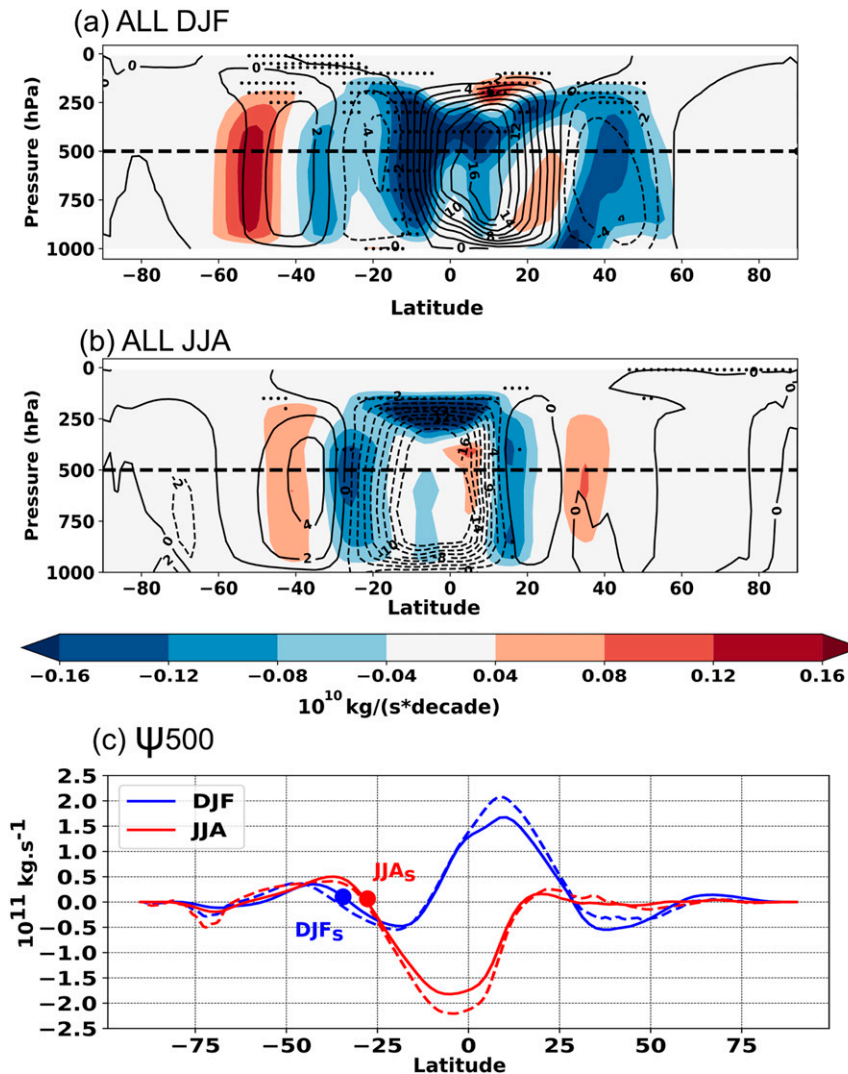


FIG. 4. Mean meridional streamfunction, in $10^{10} \text{ kg s}^{-1}$, positive clockwise, for (a) DJF and (b) JJA for the ALL ensemble mean. The black contour corresponds to the climatological values with contours every $2 \times 10^{10} \text{ kg s}^{-1}$. The color shading shows the trend in $10^{10} \text{ kg s}^{-1}$ per decade for the 1980–2014 period. Stippling denotes regions where at least 90% of the ensemble members have anomalies of the same sign. The horizontal dashed lines locate the 500-hPa level. (c), (d) Mean climatological meridional streamfunction at 500 hPa (ψ_{500}) for the 1941–61 period for ALL (thick solid lines) and ERA-I (dashed lines) in DJF (blue) and JJA (red). The dots locate the southernmost (DJFs, JJAs) boundaries of the Southern Hemisphere Hadley cell (see text for details).

(hereafter relative SST trends, similar to, e.g., Vecchi and Soden 2007). The ERA-I SST displays an extended coastal cooling in both seasons (Figs. 5a,b), with a maximum negative trend off Chile between 35° and 43°S in DJF, and off Peru between 10° and 27°S in JJA. In ALL, the cooling trend off the South American coast occurs between 20° and 35°S during both seasons (Figs. 5e,f). Although the cooling trend pattern in ALL broadly agrees with that of the observed negative SST trend, it is shifted northward by about 5° in DJF and southward by 5° in JJA. Consistent and significant southerly (i.e., upwelling-

favorable) wind stress trends develop off Chile in DJF and off north Chile and south Peru in JJA in ERA-I and ALL, albeit with a 4 times stronger amplitude in ERA-I. The amplitude difference is probably related to ensemble averaging, which damps the internal climate variability by a factor of \sqrt{n} in an n -member ensemble. Such positive wind stress trends are, however, located at the poleward boundaries of their climatological pattern, suggesting a southward extension of the southerly wind regime, in agreement with other CMIP5 climate change projections (Rykaczewski et al. 2015; Wang et al. 2015).

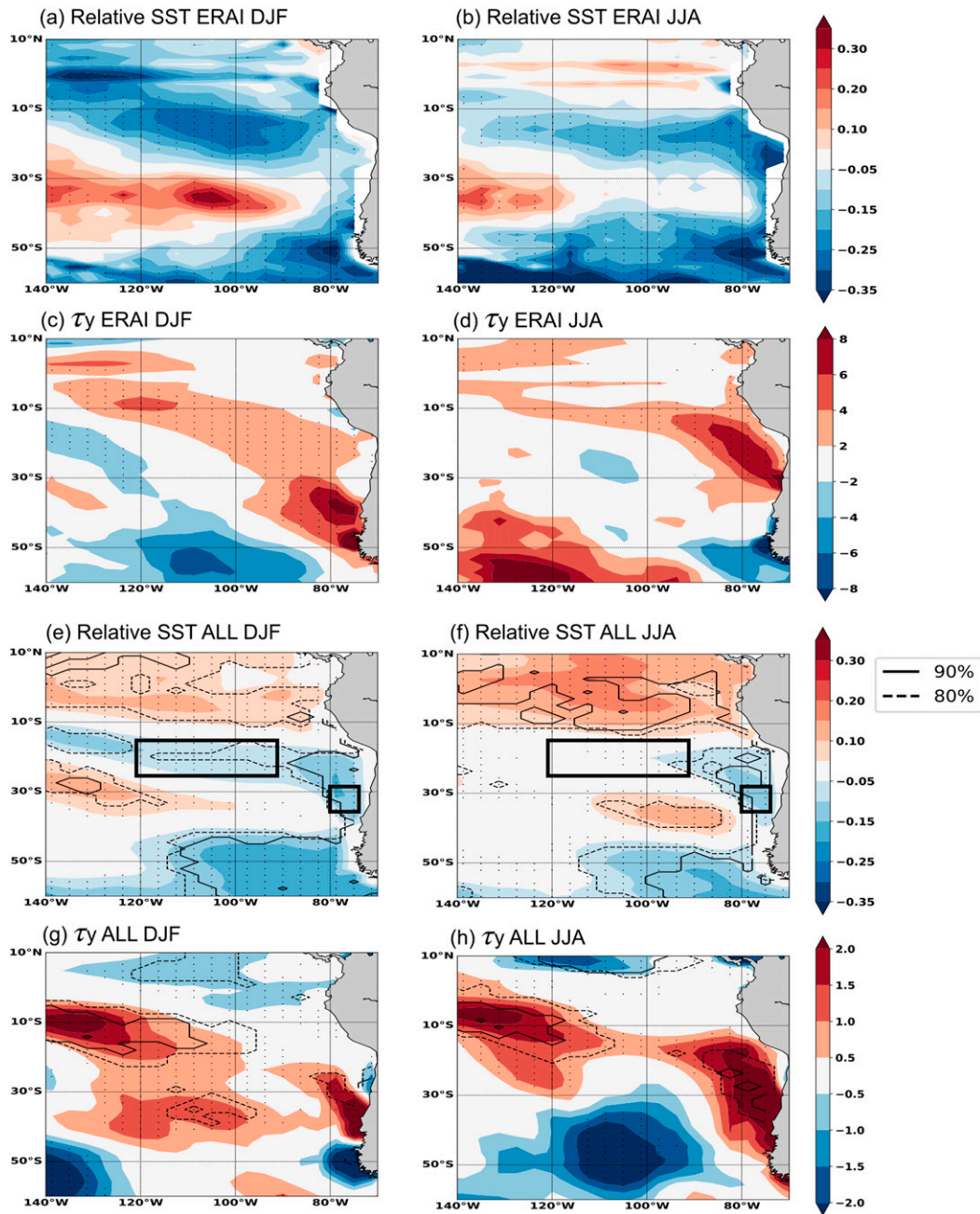


FIG. 5. ERA-Interim (a),(b) relative sea surface temperature (SST in $^{\circ}\text{C}$ per decade) and (c),(d) meridional surface wind stress (τ_y , in 10^{-1} Pa per decade) trends for the 1980–2014 period in DJF and JJA. (e)–(h) As in (a)–(d), but for the relative SST in ALL ensemble mean. Note that the meridional surface wind stress trends in ALL [(g),(h)] are 4 times weaker than ERA-I. Stippling denotes regions where the mean trends are significant at the 90% level. The black contour lines in (e)–(h) indicate where at least 80% (dashed lines) and 90% (solid lines) of the ALL member's trends have the same sign as the ensemble mean trend. The black boxes in (e),(f) correspond to the SEP and off-Chile regions used for the heat budget analyses in section 6.

Despite differences in amplitude and location that can be attributed to a combination of model biases and ensemble-averaging that damps the influence of internal variability in ALL, both observations and our model

results qualitatively agree on the southerly wind stress trend off Chile. Such trend may have enhanced the upwelling and drive the observed coastal and offshore cooling.

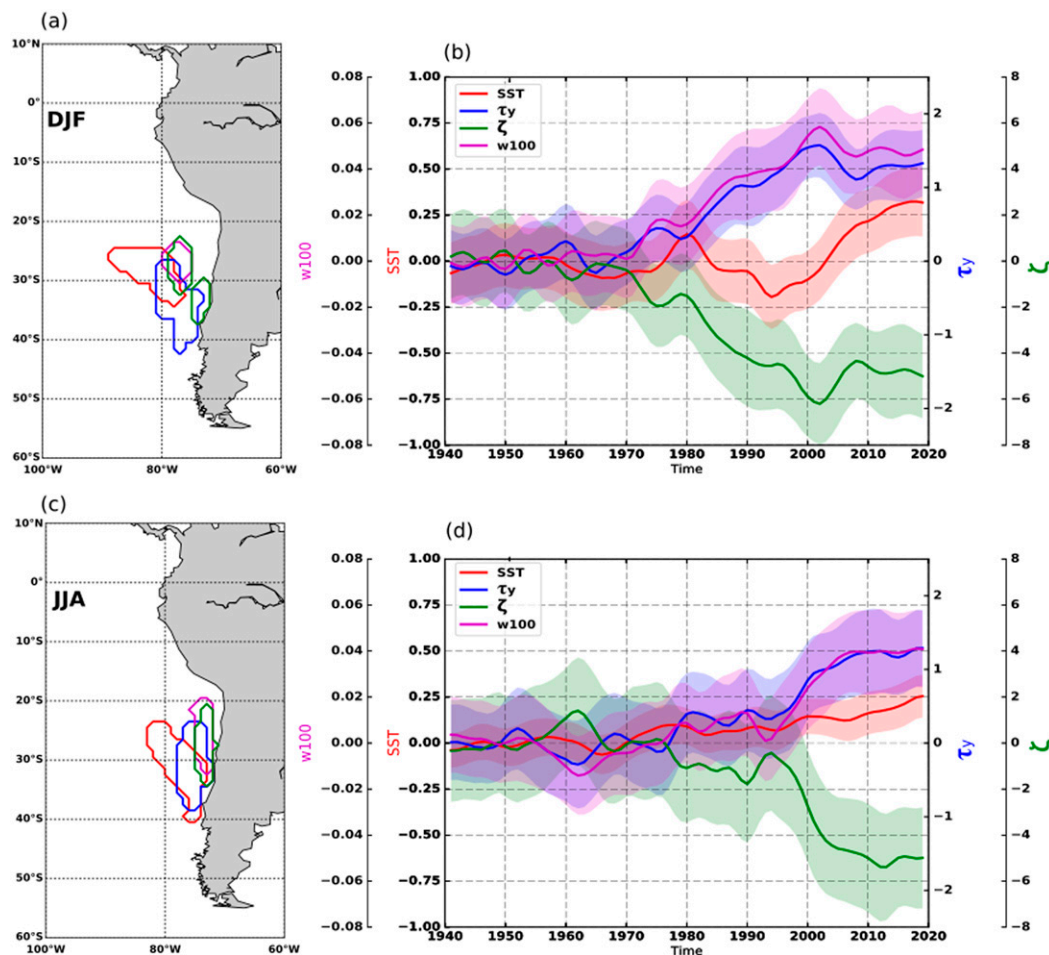


FIG. 6. Area averaged meridional surface wind stress (τ_y , blue, in 10^{-2} N m^{-2}), sea surface temperature (SST, red, in $^{\circ}\text{C}$), wind curl (ζ , green, in 10^{-9} N m^{-3}), and vertical velocity at 100-m depth in the ocean (W100, purple, in m day^{-1}) for ALL in (b) DJF and (d) JJA. Thick solid lines indicate the ensemble means; shading shows the 95% confidence interval. The regions used for the area average are shown in (a),(c), colored, respectively, as the variables (see section 2c).

Figure 6 displays the time evolution of variables that characterize the variations of the upwelling off central Chile. The dynamical variables have physically consistent variations during both seasons, with southerly (positive) wind stress, negative wind stress curl, and positive ocean velocities all consistent with an enhanced wind-driven upwelling (Figs. 6b,d). In DJF, these variables start evolving around the mid-1970s to reach a new steady state with higher mean values around 2000 (Fig. 6b). While those dynamical parameters clearly point to an increased upwelling in response to the external forcing, the picture is less clear for SST that remains relatively steady in the 1980s but then warms from the mid-1990s onward. This may be due to the compensation between the cooling driven by the enhanced upwelling of cold subsurface water and warming due to positive radiative forcing. In austral winter (JJA), the upwelling enhances more clearly from

the late 1990s onward, when SST has already started rising due to the radiative forcing (Fig. 6d). It is also reasonable to hypothesize that cooling due to the increase of the upwelling is partly counterbalancing the radiatively forced SST increase during this season as well. We will investigate this hypothesis in more detail in section 6.

b. Relative roles of forced versus internal variability on simulated regional trends

In this subsection, we characterize the relative contributions of externally forced and internal variability on decadal and multidecadal variations in the Pacific in our model. In ALL we rely on an empirical orthogonal function (EOF) analysis of SST, sea surface height (SSH), and zonal (τ_x) and meridional (τ_y) wind stress in the Pacific sector between 60°N and 50°S (Fig. 7). Figure 7a displays the PC time series obtained from projecting

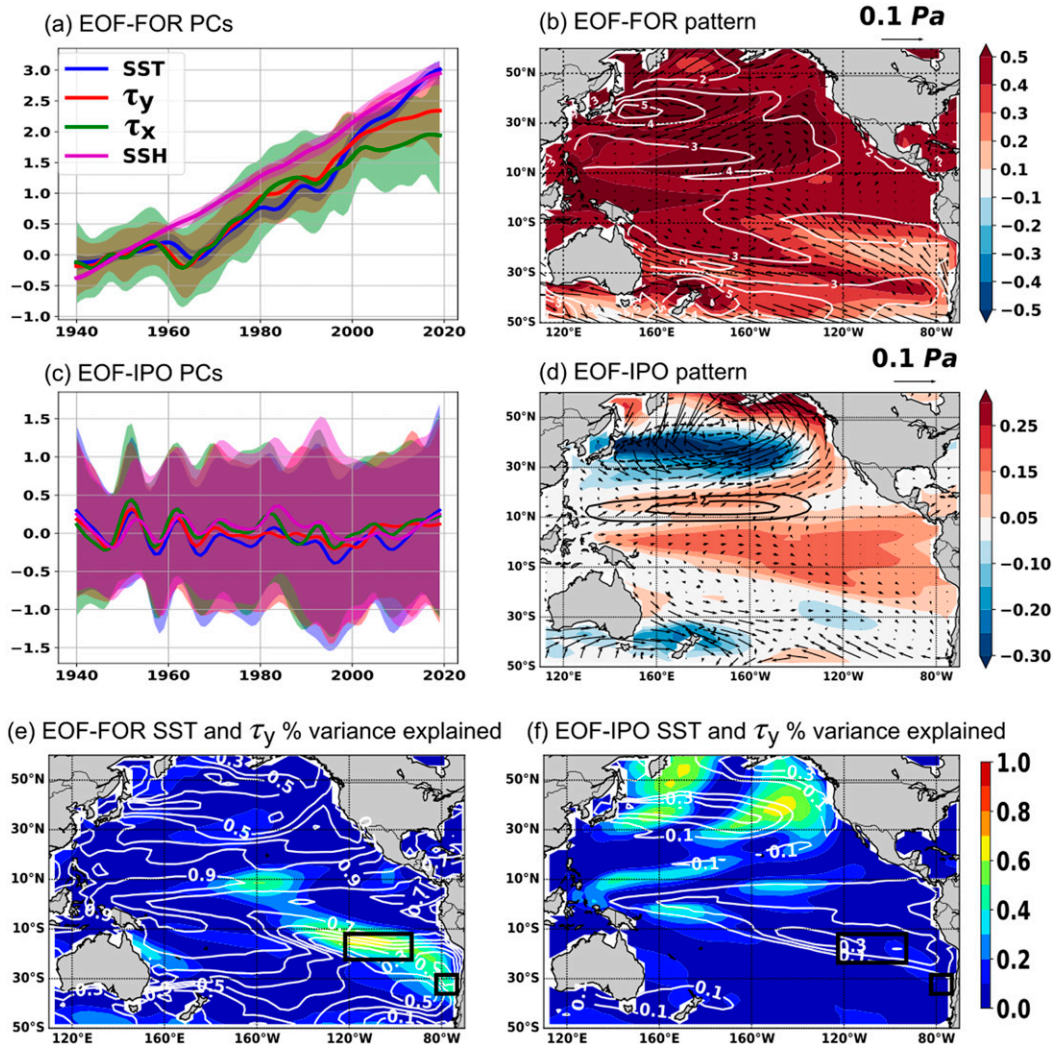


FIG. 7. EOFs and associated standardized PCs for ALL sea surface temperature (SST, in blue), meridional surface wind stress (τ_y , red), zonal surface wind stress (τ_x in green), and sea surface height (SSH in purple) derived from (a),(b) the leading ensemble mean EOF for each variable (EOF-FOR, capturing 80%–98% of the ensemble mean variations) and from (c),(d) the leading EOF of the residual (EOF-IPO) obtained after removal of the forced components. Shading in (a) and (c) shows the 90% confidence interval. (b) The regression pattern for the EOF-FOR and (d) the EOF-IPO PCs for each variable on the corresponding field anomalies of SST (color shading, in $^{\circ}\text{C}$), surface wind stress (arrows, in 0.1 Pa), and SSH (in m; contours). The percentage of variance explained by the reconstructed τ_y (shading) and SST (white contours) field using the corresponding EOF-FOR and EOF-IPO PCs for the 1980–2014 period are shown in (e) and (f), respectively. The white and black contours in (b) and (d) for SSH, are in meters per standard deviation. The black boxes in (e),(f) correspond to the SEP and off-Chile regions used for the heat budget analyses in section 6.

each ensemble member on the first EOF of ALL ensemble mean (Fig. 7b; hereafter EOF-FOR), that is, a robust estimate of the model externally forced response. EOF-FOR explains 98%, 78%, 88%, and 98% of the total variance of the ensemble-mean SST, τ_y , τ_x , and SSH, respectively (Fig. 7a; the ensemble mean and spread are displayed). We then isolated the leading mode of internal variability (EOF-IPO) by applying an EOF analysis of ALL individual members residuals, after

removing signals associated with EOF-FOR (Figs. 7c,d). The first PCs from EOF-IPO (Fig. 7c) explain 29% of the ensemble total variance for SST and τ_y , 26% for SSH, and 22% for τ_x , respectively. The related PCs exhibit a much larger spread than the first EOF-FOR PCs, as expected from internally generated climate variability. Their spatial pattern (Fig. 7d) strongly projects onto that of the IPO, the leading mode of observed internal variability at decadal time scale (Deser et al. 2010). This procedure is used to

separate the forced signal (EOF-FOR) from the leading mode of internal variability at decadal scale (EOF-IPO).

The forced surface wind stress, SST and SSH evolutions obtained from EOF-FOR (Figs. 7a,b) are consistent with Fig. 1d, and display enhanced trade winds over the central equatorial Pacific. Our model results contrast with the majority of CMIP3/5 scenario simulations that rather project a weakened Walker circulation and an El Niño-like response pattern, with the central and eastern equatorial Pacific SST warming more than the western equatorial Pacific in response to anthropogenic climate change (e.g., Collins et al. 2005; Held and Soden 2006; Kociuba and Power 2015). The SSH also rises more in the western Pacific in our model, in response to the strengthened equatorial trades.

In our region of focus, EOF-FOR reveals a weaker SST warming than in other regions and a wind strengthening in an oblique band from the Chilean coast to the central equatorial Pacific (Fig. 7b). In ALL, the forced component of the simulated variability accounts for more than 60% of the upwelling-favorable meridional wind stress (τ_y) increase (Fig. 7e) and about 20% of SST decadal variability locally off Chile (white contours in Fig. 7e). In contrast, internal variability related to IPO has no significant contribution to meridional wind stress and SST variability off Chile (Fig. 7f), but mostly contributes to these variables in the North Pacific. Farther offshore in the SEP box, the SST internal decadal variability is more important (Fig. 7f), the IPO explaining 10%–20% of SST variance while the forced component accounts for more than 40% (Fig. 7e). This analysis hence indicates that in our model IPO-related SST changes are weak relative to the forced changes in the SEP region, and very weak in the Chile upwelling region.

c. Relative roles of forced versus internal variability on observed regional trends

To evaluate the robustness of our model results and provide an estimate of the relative roles of external forcing and the IPO in observations, Figs. 8a–c display the regressed SST, surface winds, and sea level pressure (SLP) fields onto indices of the global warming signal (globally averaged SST) and IPO for the 1940–2014 period. The results reveal the imprint of the radiatively induced global warming except in North Pacific, southern Pacific, and off the Chilean coast where there is no warming signal. The global mean SST explains 1%, 32%, and 53% of the total variance for SST, meridional winds, and SLP, respectively, off Chile while the IPO explains 23% of SST variance and 1% of variance on average for both meridional winds and SLP variables (Figs. 8d–g). Farther offshore in the SEP region, the SST internal decadal variability related to IPO explains 37%,

30%, and 37% of SST, meridional winds and SLP variance, respectively, while the forced component accounts for 19%, 5%, and 17%. This analysis hence suggests that IPO-related upwelling-favorable meridional winds and related SLP changes in the Chile upwelling region are not significant, the coastal region being dominated by the forced changes while farther offshore in the SEP box, the SST internal decadal variability plays a more important role. These results are robust when the analysis is performed over a shorter, better-observed period (1960–2014; not shown). This analysis supports our conclusions based on our model large ensemble that the relative cooling off Chile and in the SEP might be tightly linked to the anthropogenic external forcing signal, which probably exerts a dominant role in reinforcing the coastal upwelling.

To further evaluate the role of the IPO phase on 1980–2014 regional SST trends in our model and observations, we show relative SST (RSST) trends in the SEP and off-Chile regions separately for ensemble members with a positive or negative IPO trend during the period (about half of the members for each, Fig. 9a). In observations, the negative IPO trend ($-0.29^\circ\text{C decade}^{-1}$; green vertical dashed line in Fig. 9a) is associated with a significant relative cooling trend both off Chile ($-0.17^\circ\text{C decade}^{-1}$) and in the SEP box ($-0.14^\circ\text{C decade}^{-1}$) regions (Figs. 9b,c; green vertical dashed line). In the model, however, the phase of the IPO does not have a clear fingerprint on local nor regional RSST trend. A significant RSST decrease off Chile ($-0.20^\circ\text{C decade}^{-1}$) and in SEP ($-0.12^\circ\text{C decade}^{-1}$) is simulated and its amplitude is consistent with observations, regardless of the IPO phase. This suggests again that the internally generated SST decadal variability is overwhelmed by the external forcing influence in ALL during the period 1980–2014. External forcing therefore likely influences the observed 1980–2014 trend.

Overall, this section demonstrates that the strengthening of the southerlies over recent decades is dominated by external forcing, both at the coast and offshore. The relative cooling trend is also dominated by external forcing in the Chile upwelling and SEP regions, with a larger contribution of internal variability (including the IPO) in the SEP. In the following section, we will relate this southerly wind anomaly to the Hadley cell extension and attribute this extension to specific external forcing.

5. Influence of the HC meridional extension and attribution to individual forcing

a. Connections between the HC and the PCUS

The strengthening of upwelling-favorable winds off Chile can be explained by large-scale atmospheric circulation changes. The climatological low-level atmospheric circulation in the PCUS region is associated with the

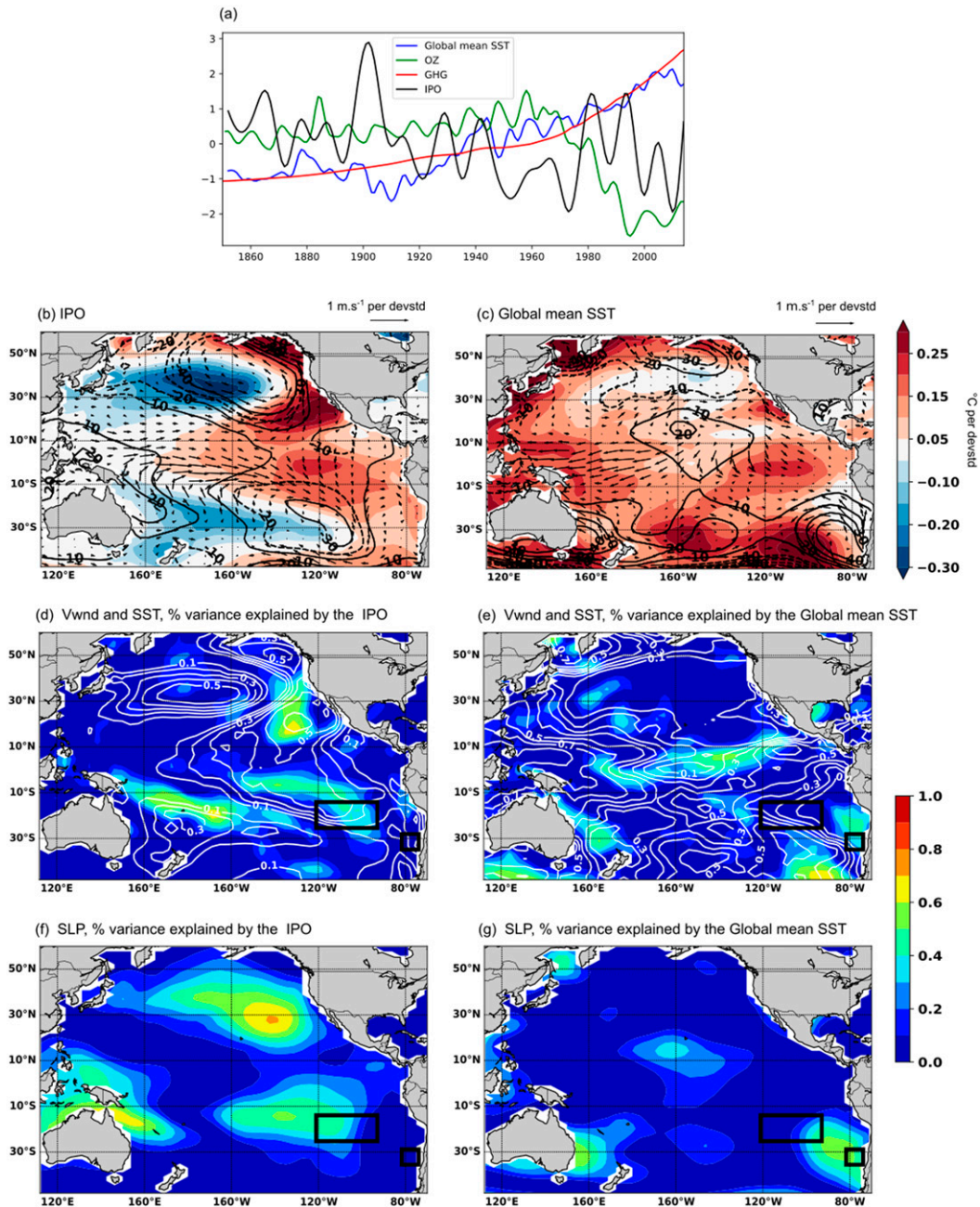


FIG. 8. (a) IPO (black curve; tripole index see section 2d), global warming signal (blue curve; globally averaged SST), atmospheric GHG (red curve; as provided by CMIP6), and stratospheric ozone (green curve; as provided by CMIP6) standardized indices for the 1940–2014 period. (b) The regression pattern on the IPO and (c) the global mean SST standardized indices on field anomalies of SST (ERSSTv4 dataset; color shading, in °C), 10-m winds (from NOAA-20C reanalyses; vectors, in $m\ s^{-1}$), and sea level pressure (SLP, from NOAA-20C reanalyses; contours, in Pa). The percentage of variance explained for the meridional 10-m wind (color shading), SST (white contours), and SLP (color shading) field using the IPO and global mean SST indices are shown in (d),(f) and (e),(g), respectively. The black contours in (b) and (c) for SLP are in Pa per standard deviation. The black boxes in (d)–(g) locate the SEP and off-Chile regions.

eastern flank of the South Pacific anticyclone (SPA; Figs. 10a,b, black contours). We now evaluate the following hypotheses for explaining the development of externally forced southerly anomalies in the PCUS

region: either a southward expansion of the HC and southward shift of the SPA (e.g., Belmadani et al. 2014) or strengthening of the land-ocean sea level pressure contrast in the context of climate change (Bakun et al. 2010).

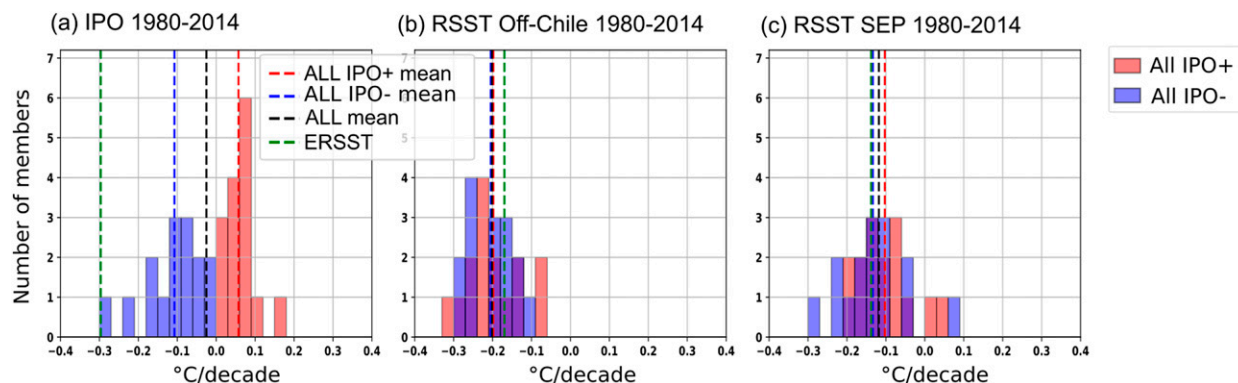


FIG. 9. Probability density function (pdf) for (a) the IPO index trends during 1980–2014 ($^{\circ}\text{C decade}^{-1}$). We computed the IPO index [relying on the tripole index (TPI) from Henley et al. (2015)], defined as the central equatorial Pacific SST (10°S – 10°N , 170°E – 90°W) minus the average of northwest (25° – 45°N , 140°E – 145°W) and southwest (15° – 50°S , 150°E – 160°W) Pacific SST, smoothed using a 13-yr Chebyshev low-pass filter (see section 2d). We then use this index to build a pdf of 34-yr-long IPO index trends allowing to split between positive (red bars) and negative (blue bars) trends. (b) As in (a), but for the relative sea surface temperature (RSST) trends (in $^{\circ}\text{C decade}^{-1}$) off Chile. (c) As in (b), but in SEP. The off-Chile and SEP regions used for the SST area-averaged in (b) and (c) are shown as black rectangles in Figs. 5 and 7. The vertical dashed lines in (a)–(c) correspond to ALL ensemble mean (black) and the mean for positive (red bars) and negative (blue bars) IPO index trends. The green vertical dashed lines correspond to ERSSTv4 trends. Note we use relative SST anomalies, respectively, to the global mean SST for both ERSSTv4 and ALL (see text).

We isolate regions of homogeneous variability of meridional wind stress and vertical velocity at 100-m depth off Chile to build area-average low-pass-filtered time series for both variables (colored contours in Figs. 10a and 10b; see section 2d). Figures 10a and 10b display the regression of the SLP anomalies onto the low-pass-filtered meridional wind stress time series off Chile in ALL (Figs. 10a,b). Southerly wind anomalies off Chile since the 1970s (1990s) in DJF (JJA) are associated with positive SLP anomalies in the southern edge of the SPA, consistent with the HC poleward expansion in other CMIP5 models (e.g., Min and Son 2013; Choi et al. 2014; Nguyen et al. 2015). The ALL ensemble mean, however, does not reproduce a decline of SLP inland over South America, as would be expected from the Bakun et al. (2010) mechanism.

To further illustrate the relationship between the Southern Hemisphere HC edge (see section 3d) and the SPA, we define an area-averaged low-pass-filtered SLP index, using box average over the region outlined on Figs. 10a and 10b (yellow box). The high correlation (0.98 and 0.96 in DJF and JJA, respectively) between the latitudinal position of the southern edge of the HC (as defined in section 3d) and the SPA SLP further illustrates the strong link between the HC southward expansion and SPA strengthening (Fig. 10c). We also find strong relations between the SPA SLP and the low-pass-filtered time series of the velocity at 100-m depth (upwelling intensity) off Chile (correlation values of 0.97 and 0.98 in DJF and JJA, respectively, Fig. 10d).

Overall, analyses in this subsection illustrate a strong link between the simulated positions of the HC southern

boundary, the intensification of the SPA, the southerly winds, and the strengthened coastal upwelling off the Chilean coast.

b. Attribution of HC variations to individual external forcing

Figure 11 displays the time series of the ensemble-mean latitude of the Southern Hemisphere HC poleward edge in ALL, GHG, and OZ during 1940–2020 and in twentieth-century NOAA–CIRES (Compo et al. 2011), NCEP (Kalnay et al. 1996), and ERA-I (Dee et al. 2011) reanalyses. The reanalyses and ALL ensemble mean all reveal (with the exception of NCEP in JJA) a significant poleward shift of the subsiding branch of the Hadley cell, from the 1970s onward with a stabilization during the last two decades of the simulated period. The shift is more pronounced in DJF ($\sim 0.8^{\circ}\text{S}$ in 1980–2014) than in JJA ($\sim 0.45^{\circ}\text{S}$). ALL results are within the range of reanalyses uncertainties, which indicate a 0.25° to 3° poleward expansion of the HC southern edge since the seventies (Figs. 11c,d; Seidel and Randel 2007; Staten et al. 2018; Grise et al. 2019).

Single-forcing experiments suggests that volcanic forcing does not contribute to the HC southward expansion (Figs. 11a,b). During austral winter (JJA), the ozone contribution is also weak, and the greenhouse gas forcing dominates the HC expansion, producing a linear trend in the HC poleward expansion, from 1970 to 2020 (Fig. 11b). GHG and stratospheric ozone depletion both act to expand the HC in austral summer, the impact of ozone depletion dominating before 1995 in agreement with previous studies (e.g., Min and Son 2013;

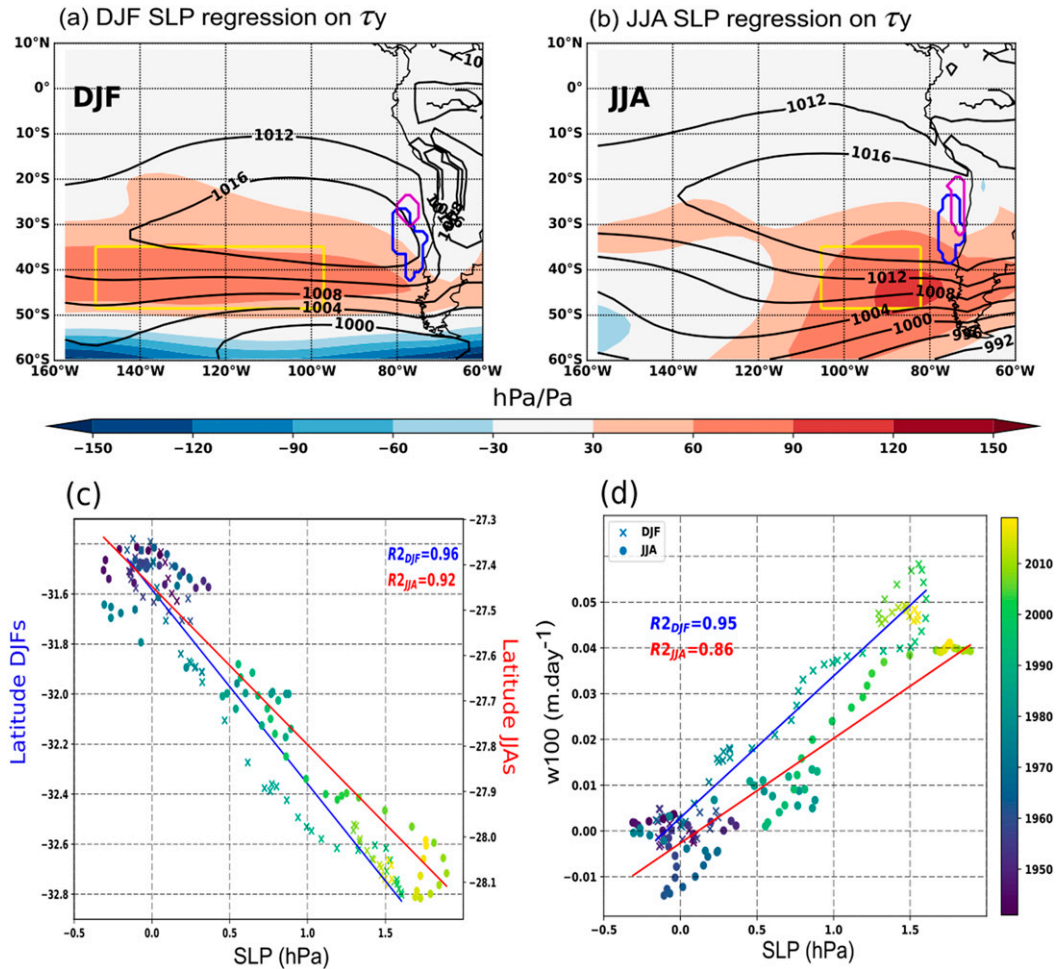


FIG. 10. Sea level pressure (SLP) 1941–61 climatology (black contours, every 4 hPa) and linear regression (shading, in hPa Pa^{-1}) of the SLP on the mean meridional surface wind stress off Chile in (a) DJF and (b) JJA for the 1980–2014 period using ALL Ensemble mean. (c) Scatterplot between the latitudinal positions of the Southern Hemisphere Hadley cell boundaries vs the area averaged South Pacific sea level pressure (SLP, in hPa) anomalies in DJF (DJFs, crosses) and JJA (JJAs, dots). (d) Scatterplot between vertical velocity at 100-m depth (w_{100} , in m day^{-1}) off the Chilean coast with the area averaged South Pacific SLP anomalies (in hPa) in DJF (crosses) and JJA (dots). The scatterplots are using values from ALL ensemble mean. The coefficient of determination (R^2) between each variable is given in (c),(d). The dots and crosses in (c),(d) are colored from the oldest (dark blue) to the most recent years (yellow) of the simulation for the whole 1940–2020 period. The blue and red lines show the regression lines in DJF (blue) and JJA (red). The yellow box in (a),(b) corresponds to the regions used for the SLP South Pacific anticyclone. The blue and purple contours in (a),(b) indicate the region used for the area average of meridional surface wind and w_{100} off Chile.

Waugh et al. 2015). After 1995, the ozone recovery (Szopa et al. 2013) yields a stabilization of the ozone contribution to the HC expansion, at a level similar to that of GHGs. Together, these two effects yield an austral summer HC meridional expansion from 1970 to 2000, followed by stabilization from 2000 onward.

c. Attribution of PCUS variations to various external forcing

Since all the variables that characterize the PCUS are highly correlated (see section 4a), Fig. 12 displays only

SST and w_{100} (hereafter upwelling) anomalies in single-forcing ensemble simulations. The (GHG + VOLC + OZ) mean SST and w_{100} time series fit well with the ALL curve, suggesting a linear additivity of each individual externals forcings. Increased upwelling caused by the ozone depletion (Fig. 12a) explains most of the SST cooling visible in the early 1980s in DJF (Fig. 12c). The SST variations in OZ hence largely reflect wind-driven changes linked to stratospheric ozone changes. These effects of the ozone forcing start decreasing after 1995 in association with the ozone recovery. GHG contributes

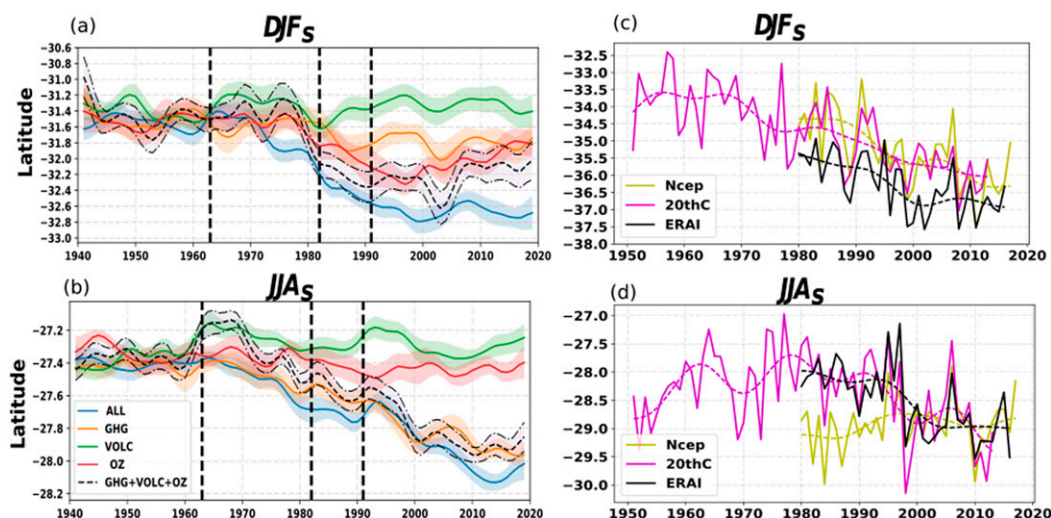


FIG. 11. Time series of the poleward edge of the Southern Hemisphere Hadley cell in (a) December–February (DJFs) and (b) June–August (JJAs) for ALL (blue), GHG (orange), VOLC (green), and OZ (red). Colored thick solid lines indicate the ensemble means, shading shows the 95% confidence interval. The sum between GHG, VOLC, and OZ is shown as a black dashed curve. The vertical dashed lines indicate the timing of Agung (March 1963), El Chichón (April 1982), and Pinatubo (June 1991) eruptions. (c),(d) As in (a),(b), but for NCEP (in yellow), NOAA-CIRES 20CR (in pink), and ERA-I (in black) reanalyses. Solid thick lines correspond to the annual time series and dashed lines after applying a 7-yr Hanning filter.

mainly to upwelling changes in JJA (Fig. 12b) through dynamically induced cooling but this is overwhelmed by radiatively induced warming (Fig. 12d). Hence the two competing effects between cooling through strengthened upwelling and warming through GHGs, radiative effect sustain the relatively limited surface warming off Chile as compared to the surrounding regions (Fig. 1). Even if the volcanic forcing contributes through a small weakening after Agung (March 1963), El Chichón (April 1982), and Pinatubo (June 1991), we clearly see a dynamical response with an upwelling intensification in response to the anthropogenic forcing during both seasons. GHG and OZ forcing within ALL combine to produce the upwelling intensification since the 1970s. This upwelling intensification first counteracts the effect of the GHGs radiative forcing, leading to a stable SST until ~ 2000 . After the ozone recovery, the forcing from GHGs overwhelms the cooling effect of the enhanced upwelling, yielding a SST increase. Overall, this is consistent with the weaker SST increase off Chile than in surrounding regions, in response to radiative forcing. In the following section, we further investigate this surface warming using a simplified heat budget of the upper oceanic layer.

6. Why does the southeast Pacific warm less than the rest of Pacific Ocean?

We contrast the SST upper ocean budget of our two regions of interest, namely nearshore off Chile (32° – 30° S,

80° – 75° W) and farther offshore in the subtropical SEP (25° – 17° S, 120° – 90° W; Fig. 13a), with that of the entire Pacific (50° S– 50° N, 120° E– 75° W), in order to elucidate why these two regions warm at a reduced rate. The average Pacific warming starts 20 years earlier in the 1970s and is larger ($+1.2^{\circ}$ C in 2020) than that of the SEP ($+0.6^{\circ}$ C) and off-Chile ($+0.2^{\circ}$ C) regions (Fig. 13b). The contributions from the surface heat flux (labeled ATM; first term in the rhs of Eq. (1) in section 2d) and the oceanic processes (labeled OCE_{dyn} , second term in the rhs of Eq. (1), including lateral and vertical advection and mixing) are detailed in Fig. 13c.

At the scale of the Pacific Ocean (Fig. 13c, red curves), the GHG forcing induces a positive net air–sea flux (dominated by downward longwave radiation, not shown) that warms the ocean, as expected from the effect of greenhouse gases (e.g., Barnett et al. 2005). A cooling by oceanic processes largely compensates this warming. The climate change induced warming indeed occurs predominantly in the ocean surface layer (e.g., Barnett et al. 2005), and hence increases the temperature difference between the surface layer and the subsurface, and thus the cooling by turbulent fluxes at the bottom of the mixed layer. In the nearshore region, the warming is also due to atmospheric heat fluxes, but partly compensated by a larger cooling due to increased upwelling. This is supported by Fig. 13c (blue curves), which reveals a stronger cooling by oceanic processes in the off-Chile region (presumably largely because of

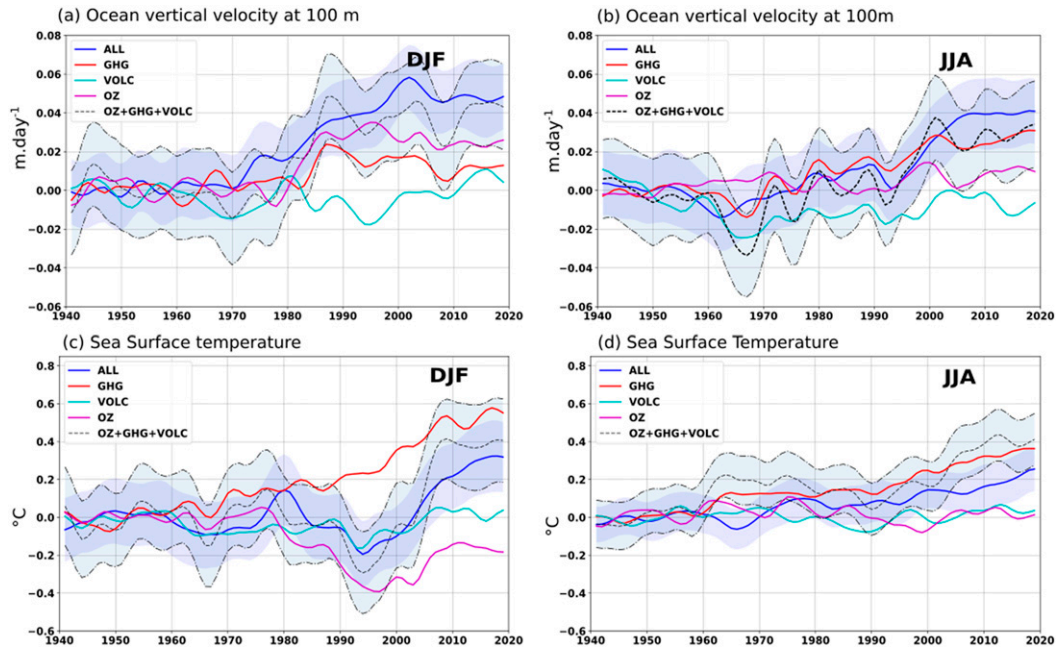


FIG. 12. (a),(b) Off-Chile vertical velocity at 100-m depth (in m day^{-1}) and (c),(d) sea surface temperature (in $^{\circ}\text{C}$) in DJF and JJA for ALL (blue), GHG (red), VOLC (green), and OZ (purple). The regions for the area average off Chile are shown as purple and red contours in (a) and (c) of Fig. 6. The sum between GHG, VOLC, and OZ is shown as a black dashed curve and dashed-dotted lines. Colored thick solid lines indicate the ensemble means; shading shows the 95% confidence interval.

changes in upwelling) than over the entire Pacific (presumably largely because of changes in thermal stratification and vertical mixing of heat). Figure 13f displays upward velocity and cooling trends in the top 500 m near the coast off Chile that supports this view.

It is intriguing that in the offshore SEP region the warming rate is also less than for the Pacific average since it is not an upwelling region (Fig. 13b, green curve). There, the impact of atmospheric net air–sea heat fluxes trend [Q_{atm} in Eq. (2)] is almost nearly neutral (Fig. 13d, green dashed line) due to a balance between increased longwave radiations [Q_{lw} in Eq. (2)] contributing to warming ($6.28^{\circ}\text{C decade}^{-1}$ during 1980–2014) and the negative trend of net shortwave radiations at ocean surface [$Q_{\text{sw}} - Q_{\text{swh}}$ in Eq. (2); $-4.25^{\circ}\text{C decade}^{-1}$ during 1980–2014], assuming a fixed climatological mixed layer depth. Indeed, more low-level clouds are increasingly formed over the SEP region (not shown), due to relatively colder SST and boundary layer stratification under the synoptic HC descent over the SEP region (Bony et al. 2006), which results in a local planetary albedo increase. The strengthening of the surface wind anomalies also favors cooling through enhanced latent heat flux ($-4.03^{\circ}\text{C decade}^{-1}$ during 1980–2014), while sensible heat fluxes anomalies explain a small warming ($+0.63^{\circ}\text{C decade}^{-1}$ during 1980–2014). Near the coast,

however, low-level cloud cover decreases in response to a stronger southerly coastal jet in our simulations. This is consistent with the observed synoptic-scale covariability of surface winds and low cloud cover off Chile at 33°S (Garreaud and Muñoz 2005). Consequently, the downward shortwave flux is more intense near the coast than offshore, resulting in a larger Q_{atm} . Wind stress strengthening over SEP and coastal regions (Figs. 5g,h) also influences the mixed layer depth and hence could modulate the atmospheric heat fluxes impact on SST.

The respective roles of the mixed layer thickness (h) and net surface downward heat flux (Q) variations in ATM can be evaluated by fixing either h or Q to their climatological values (Fig. 13d). Whereas SST increases in the three considered regions, the mixed layer depth increases during 1960–2000 particularly in DJF at rates over 0.9 and $0.7 \text{ m decade}^{-1}$ in the SEP and nearshore regions, respectively, whereas no changes is evidenced on average over the Pacific basin (figures not shown). The annual-mean surface net heat flux in the SEP region being positive (4.80 W m^{-2} in ALL), a thickening of the mixed layer (and hence higher mixed layer heat capacity) results in a decrease of heating rate by surface heat fluxes ($-5.18^{\circ}\text{C decade}^{-1}$ during 1980–2014; green solid curve in Fig. 13c; green crossed line in Fig. 13d) (i.e., an anomalous cooling).

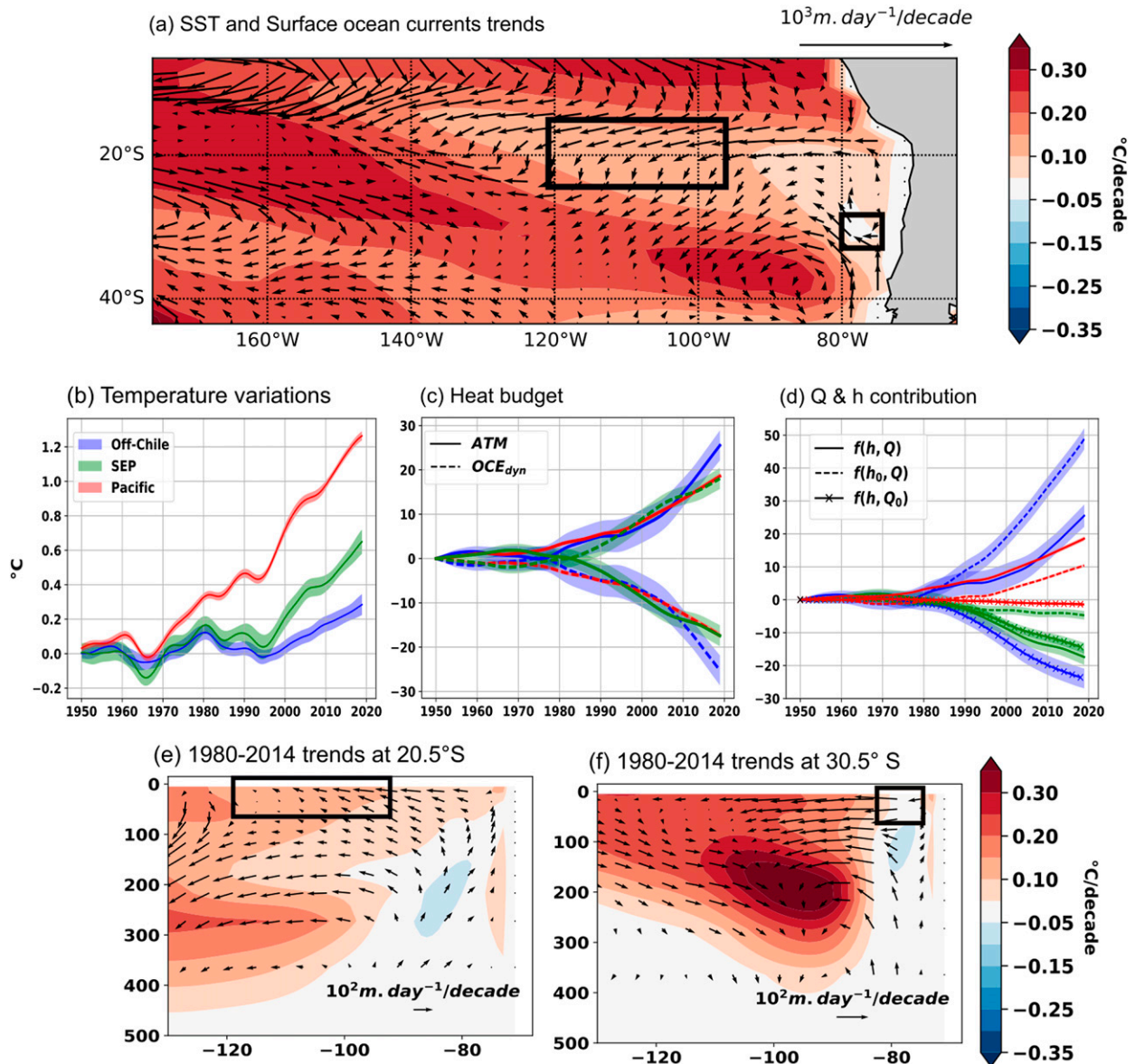


FIG. 13. ALL (a) ensemble mean trends of sea surface temperature (SST, shading, $^{\circ}\text{C decade}^{-1}$) and surface current (arrows, $10^3 \text{ m day}^{-1} \text{ decade}^{-1}$) over 1980–2014, (b) sea surface temperature anomalies, and (c) integrated net mixed layer heat budget for the Pacific basin (red curves), southern Pacific (SEP, green curves), and off-Chile (blue curves) regions. The regions used for the SEP and off-Chile area averages are shown as black boxes in (a). In (c) the thick solid lines correspond to the influence of heat flux (ATM) and the dashed lines to the influence of oceanic processes (OCE_{dyn}); see section 2e for details. (d) Influence of heat flux considering both heat flux (Q) and mixed layer (h) variations (thick solid lines), only Q (dashed lines), or only h variations (crossed lines). The h_0 and Q_0 in the legend indicate that the climatological value is used for the calculation. Thick lines indicate the ensemble means while shading shows the 90% confidence interval. (e),(f) Vertical section of potential temperature (color shading, $^{\circ}\text{C decade}^{-1}$) and velocity (arrows, $10^2 \text{ m day}^{-1} \text{ decade}^{-1}$) trends over 1980–2014 period off Chile at 30.5°S and in SEP region at 29.5°S, respectively, for the ALL ensemble mean. A scaling factor of 1.4×10^4 off-Chile and 1.6×10^4 in SEP is applied on the vertical velocity.

In contrast, the ocean processes in the SEP contribute to an anomalous warming trend (green dashed curve in Fig. 13c). This can be explained neither by changes in vertical velocities nor mixing, because these changes (upwelling tendency and larger warming near the surface, Fig. 13e) would rather be conducive to

cooling. This suggests that changes in lateral advection drive the warming. The SEP reduced warming with respect to its surroundings (Fig. 13a) implies a warming trend due to the advection of anomalous SST by mean surface currents. The currents' changes also involve a southward component (due to Ekman transport,

Fig. 13a) that increases the southward advection of warmer water from farther north.

7. Discussion and conclusions

A SST cooling trend is observed off northern Chile since 1980 and off southern Peru since the mid-twentieth century. Bakun et al. (2010) argue that surface pressure decreases more on land than over the ocean in response to anthropogenic forcing, giving rise to upwelling-favorable winds in eastern boundary upwelling systems (EBUS), which would explain the PCUS cooling trend. The observed negative interdecadal Pacific oscillation (IPO) trend over the same period is, however, also associated with cooling in the southeastern Pacific and could contribute to the observed trend. In this study, we quantify the relative role of internal and external forcing in this trend, and the associated mechanisms. Our ensemble-mean historical simulation reproduces a weaker recent SST trend in the southeastern part of the basin than in the surroundings, with virtually no warming off Chile since the 1970s, and a southerly wind anomaly at the coast and offshore.

In line with other studies based on CMIP5 models (e.g., Wang et al. 2015; Rykaczewski et al. 2015), we find no clear low pressure trend over South America that could lead to a southerly wind and upwelling intensification. The externally forced component of the simulated variability accounts for more than 60% of upwelling-favorable meridional wind stress increase off Chile, while a negative IPO canonical internal variability pattern has no significant contribution to the meridional wind stress positive trend over the same period. In the real world the IPO has a different spatial structure, amplitude and time behavior to that in CMIP5-class models (Kravtsov 2017). Analyses of observed decadal trends in SST, wind stresses and SLP separated into the IPO and forced components are however consistent with our model results. Hence, regional and local SST cooling patterns in the SEP and off Chile might be tightly linked to the anthropogenic external forcing signal, which potentially exerts a dominant role in reinforcing the coastal upwelling. PCUS can also be modulated by coastally trapped waves remotely forced by equatorial Pacific zonal wind fluctuations (Montecinos et al. 2007). This process may also contribute to the coastal upwelling enhancement.

Previous modeling work shows that south of 33°S the poleward South Pacific anticyclone migration causes geostrophy to break down due to the Andes orographic barrier (Muñoz and Garreaud 2005; Belmadani et al. 2014), locally precluding the establishment of the geostrophic equilibrium in the alongshore direction. This

probably explains why the increase in modeled alongshore winds is rather associated with an intensification of the alongshore pressure gradient. We further link the development of these southerly wind anomalies to a poleward expansion of the Southern Hemisphere Hadley cell, and strengthened South Pacific anticyclone, from around 1980 until a new steady state is reached in austral summer 2000 and in austral winter 2010. Attribution analyses demonstrate that enhanced alongshore winds and upwelling near the Chilean coast are due to greenhouse gases and ozone anthropogenic forcings, as both contribute to shift poleward the Hadley cell southern boundary (e.g., Staten et al. 2018; Grise et al. 2019). The large tendency in the 1980s and the relatively stable steady state later are consistent with the reduced influence of stratospheric ozone after 1995. The upwelling intensification is the main driver of the negative relative SST (RSST) trend along the Chilean coast. Farther offshore, previous studies suggest that the main mechanism for the robust negative RSST trend in the SEP region is the wind–evaporation–SST (WES) feedback (e.g., Xie et al. 2010; Timmermann et al. 2010; Lu and Zhao 2012) (i.e., that stronger winds enhance evaporative cooling locally). Instead, we find a dominant role of the wind-forced mixed layer deepening, which leads to a decreased warming rate by surface air–sea fluxes.

A potential caveat of our study is the coarse spatial resolutions of both the atmospheric (1.87° in latitude and 3.75° longitude) and ocean (2° horizontal resolution of Chile) components of the IPSL-CM5A coupled model. Our coarse model resolution (similar to CMIP5 class models) does not resolve several small-scale coastal processes, such as those associated with mesoscale oceanic eddies that contribute to the offshore transport of the cold upwelled water (e.g., Colas et al. 2013), coastal capes (e.g., Renault et al. 2016), sea breeze (Franchito et al. 1998), and the intensified temperature gradient induced by the warming of the narrow plains between the coast and the high Andes off Peru and northern Chile (e.g., Garreaud and Falvey 2009). Our results are nevertheless consistent with those obtained by Belmadani et al. (2014) that used an atmospheric model at higher horizontal resolution (50 km). Relying on dynamical downscaling of global GCM climate scenarios, Belmadani et al. (2014) obtain a wind strengthening off central Chile around 30°–35°S and a weakening or no changes off Peru in agreement with regional atmospheric modeling (horizontal resolution ~45 km) works by Quijano-Vargas (2011) and Muñoz and Garreaud (2005) for central Peru and north-central Chile coastal regions, respectively. These studies did not however include coupling with the ocean. Future work with regional coupled models at higher spatial resolution will be needed to confirm the robustness of our results.

The model and observations are consistent in terms of relative SST (i.e., in displaying a cooling relative to the regional average in the SEP and PCUS). However, in terms of absolute SST, the observations indicate a slight cooling trend in the PCUS region, while the model indicates a slight warming trend. This is most likely associated with the too strong climate sensitivity of our climate model (Andrews et al. 2012; Forster et al. 2013), which results in an overestimated surface global warming that offsets the regional cooling trend. This is accentuated by the fact that aerosol forcing (which induces a global cooling trend) is omitted in our simulation. We however probably partly remove this bias by using relative SST (i.e., subtracting the overestimated global mean SST warming). Our approach relying on relative SST, observations, and large ensembles needed to explore the regional responses to internal variability and to forcing histories nevertheless allows shedding light on the intrinsic dynamics of the southeast Pacific in recent decades. Upcoming CMIP6 simulations would offer the possibility to evaluate those results in a multimodel context.

We did not discuss changes along the tropical Peruvian coast (4° – 15° S) in detail since this region does not display any clear relative SST cooling or significant changes in wind intensity in the ALL ensemble mean. Previous studies however suggest that SST trends off northern Peru are dominated by more frequent central Pacific El Niños after 1980 (Dewitte et al. 2012). Note that the analysis of observed winds also suggests no clear trend in the northern part of the Peruvian upwelling (Belmadani et al. 2014) despite the negative IPO trend during 1980–2014 (Vuille et al. 2015). Other eastern boundary upwelling systems (EBUS) of the Southern Hemisphere such as the Benguela system off southern Africa (e.g., Lamont et al. 2018) and the one west of Australia (e.g., Rousseaux et al. 2012) do not appear to show any cooling (Fig. 1). Observed SST trends during 1980–2014 in the Atlantic Ocean mainly capture a large tropical Atlantic warming (Li et al. 2016) while Indian Ocean SST displays a warming trend that may reflect the global warming signal (Dong and McPhaden 2016; Fig. 1). Dedicated studies are needed to attribute the ocean expression of the Southern Hemisphere HC expansion in other southern EBUSs, which largely depends on the local features such as bottom topography, mixed layer depth, net surface fluxes, strength of the stratification, and regional ocean currents.

To summarize, we find that GHG increase and ozone depletion over the last few decades project onto robust southeasterly wind stress and negative RSST trend patterns in the southeastern Pacific. Anthropogenic forcings dominate this negative RSST trend in our model, as

almost all the members display a weaker cooling in the southeastern Pacific than in surrounding regions (and the observed RSST trend lying within the simulated distribution). Our results suggest that GHG and ozone anthropogenic forcing are likely the key driving factors for the recent observed PCUS intensification, and that the recent negative IPO phase played little or no role in this regional trend. Considering the continuous increase in atmospheric GHG and the unexpected and persistent global emissions of stratospheric ozone-depleting CFC-11 since 2012 (Montzka et al. 2018), our results provide practical guidance for the future climate response in the PCUS.

Acknowledgments. This research was supported by the French National Research Agency under the program Facing Societal, Climate and Environmental Changes (MORDICUS Project, Grant ANR-13-SENV-0002). This work was granted access to the HPC resources of TGCC under the allocations 2016-017403 and A003017403 made by GENCI. This study also benefited from the IPSL mesocenter facility, which is supported by CNRS, UPMC, Labex L-IPSL (funded by the ANR Grant ANR-10-LABX-0018 and by the European FP7 IS-ENES2 Grant 312979). We thank the ECMWF for providing the ERA-Interim reanalysis. The OISST dataset was provided by the NOAA/OAR/ESRL PSD, Boulder, Colorado. Support for the Twentieth Century Reanalysis Project, version 2c, dataset is provided by the U.S. Department of Energy, Office of Science Biological and Environmental Research (BER), and by the National Oceanic and Atmospheric Administration Climate Program Office. NCEP reanalysis data are provided by the NOAA/OAR/ESRL PSD, Boulder, Colorado (<https://www.esrl.noaa.gov/psd/>).

REFERENCES

- Adam, O., T. Schneider, and N. Harnik, 2014: Role of changes in mean temperatures versus temperature gradients in the recent widening of the Hadley circulation. *J. Climate*, **27**, 7450–7461, <https://doi.org/10.1175/JCLI-D-14-00140.1>.
- Alexander, M. A., I. Bladé, M. Newman, J. R. Lanzante, N.-C. Lau, and J. D. Scott, 2002: The atmospheric bridge: The influence of ENSO teleconnections on air–sea interaction over the global oceans. *J. Climate*, **15**, 2205–2231, [https://doi.org/10.1175/1520-0442\(2002\)015<2205:TABTIO>2.0.CO;2](https://doi.org/10.1175/1520-0442(2002)015<2205:TABTIO>2.0.CO;2).
- Allen, R. J., and O. Ajoku, 2016: Future aerosol reductions and widening of the northern tropical belt. *J. Geophys. Res. Atmos.*, **121**, 6765–6786, <https://doi.org/10.1002/2016JD024803>.
- Andrews, T., J. M. Gregory, M. J. Webb, and K. E. Taylor, 2012: Forcing, feedbacks and climate sensitivity in CMIP5 coupled atmosphere–ocean climate models. *Geophys. Res. Lett.*, **39**, L09712, <https://doi.org/10.1029/2012GL051607>.
- Arakelian, A., and F. Codron, 2012: Southern Hemisphere jet variability in the IPSL GCM at varying resolutions. *J. Atmos. Sci.*, **69**, 3788–3799, <https://doi.org/10.1175/JAS-D-12-0119.1>.

- Aravena, G., B. Broitman, and N. C. Stenseth, 2014: Twelve years of change in coastal upwelling along the central-northern coast of Chile: Spatially heterogeneous responses to climatic variability. *PLOS ONE*, **9**, e90276, <https://doi.org/10.1371/journal.pone.0090276>.
- Bakun, A., D. B. Field, A. Redondo-Rodríguez, and S. J. Weeks, 2010: Greenhouse gas, upwelling-favorable winds, and the future of coastal ocean upwelling ecosystems. *Global Change Biol.*, **16**, 1213–1228, <https://doi.org/10.1111/j.1365-2486.2009.02094.x>.
- Balmaseda, M. A., K. E. Trenberth, and E. Källén, 2013: Distinctive climate signals in reanalysis of global ocean heat content. *Geophys. Res. Lett.*, **40**, 1754–1759, <https://doi.org/10.1002/grl.50382>.
- Barnes, E. A., and L. Polvani, 2013: Response of the midlatitude jets, and of their variability, to increased greenhouse gases in the CMIP5 models. *J. Climate*, **26**, 7117–7135, <https://doi.org/10.1175/JCLI-D-12-00536.1>.
- Barnett, T. P., D. W. Pierce, K. M. AchutaRao, P. J. Gleckler, B. D. Santer, J. M. Gregory, and W. M. Washington, 2005: Penetration of human-induced warming into the world's oceans. *Science*, **309**, 284–287, <https://doi.org/10.1126/science.1112418>.
- Bayr, T., and D. Dommenget, 2013: The tropospheric land–sea warming contrast as the driver of tropical sea level pressure changes. *J. Climate*, **26**, 1387–1402, <https://doi.org/10.1175/JCLI-D-11-00731.1>.
- Beaugrand, G., and Coauthors, 2019: Prediction of unprecedented biological shifts in the global ocean. *Nat. Climate Change*, **9**, 237–243, <https://doi.org/10.1038/s41558-019-0420-1>.
- Bellenger, H., É. Guilyardi, J. Leloup, M. Lengaigne, and J. Vialard, 2014: ENSO representation in climate models: From CMIP3 to CMIP5. *Climate Dyn.*, **42**, 1999–2018, <https://doi.org/10.1007/s00382-013-1783-z>.
- Belmadani, A., V. Echevin, F. Codron, K. Takahashi, and C. Junquas, 2014: What dynamics drive future wind scenarios for coastal upwelling off Peru and Chile? *Climate Dyn.*, **43**, 1893–1914, <https://doi.org/10.1007/s00382-013-2015-2>.
- Boer, G., G. Flato, and D. Ramsden, 2000: A transient climate change simulation with greenhouse gas and aerosol forcing: Projected climate to the twenty-first century. *Climate Dyn.*, **16**, 427–450, <https://doi.org/10.1007/s003820050338>.
- Bony, S., and Coauthors, 2006: How well do we understand and evaluate climate change feedback processes? *J. Climate*, **19**, 3445–3482, <https://doi.org/10.1175/JCLI3819.1>.
- Bopp, L., and Coauthors, 2013: Multiple stressors of ocean ecosystems in the 21st century: Projections with CMIP5 models. *Biogeosciences*, **10**, 6225–6245, <https://doi.org/10.5194/bg-10-6225-2013>.
- Brient, F., and S. Bony, 2013: Interpretation of the positive low-cloud feedback predicted by a climate model under global warming. *Climate Dyn.*, **40**, 2415–2431, <https://doi.org/10.1007/s00382-011-1279-7>.
- Capet, X. J., P. Marchesio, and J. C. McWilliams, 2004: Upwelling response to coastal wind profiles. *Geophys. Res. Lett.*, **31**, L13311, <https://doi.org/10.1029/2004GL020123>.
- Carton, J. A., and B. S. Giese, 2008: A reanalysis of ocean climate using Simple Ocean Data Assimilation (SODA). *Mon. Wea. Rev.*, **136**, 2999–3017, <https://doi.org/10.1175/2007MWR1978.1>.
- Chavez, F. P., A. Bertrand, R. Guevara-Carrasco, P. Soler, and J. Csirke, 2008: The northern Humboldt Current system: Brief history, present status and a view towards the future. *Prog. Oceanogr.*, **79**, 95–105, <https://doi.org/10.1016/j.pcean.2008.10.012>.
- Chen, S., K. Wei, W. Chen, and L. Song, 2014: Regional changes in the annual mean Hadley circulation in recent decades. *J. Geophys. Res. Atmos.*, **119**, 7815–7832, <https://doi.org/10.1002/2014JD021540>.
- Choi, J., S. W. Son, J. Lu, and S. K. Min, 2014: Further observational evidence of Hadley cell widening in the Southern Hemisphere. *Geophys. Res. Lett.*, **41**, 2590–2597, <https://doi.org/10.1002/2014GL059426>.
- Choi, J.-W., I.-G. Kim, J.-Y. Kim, and C.-H. Park, 2016: The recent strengthening of Walker circulation. *SOLA*, **12**, 96–99, <https://doi.org/10.2151/SOLA.2016-022>.
- Colas, F., X. Capet, J. C. McWilliams, and Z. Li, 2013: Mesoscale eddy buoyancy flux and eddy-induced circulation in eastern boundary currents. *J. Phys. Oceanogr.*, **43**, 1073–1095, <https://doi.org/10.1175/JPO-D-11-0241.1>.
- Collins, M., and Coauthors, 2005: El Niño- or La Niña-like climate change? *Climate Dyn.*, **24**, 89–104, <https://doi.org/10.1007/s00382-004-0478-x>.
- Compo, G. P., and Coauthors, 2011: The Twentieth Century Reanalysis project. *Quart. J. Roy. Meteor. Soc.*, **137**, 1–28, <https://doi.org/10.1002/qj.776>.
- Cushing, D. H., 1971: Upwelling and the production of fish. *Adv. Mar. Biol.*, **9**, 255–334, [https://doi.org/10.1016/S0065-2881\(08\)60344-2](https://doi.org/10.1016/S0065-2881(08)60344-2).
- de Boissésou, E., M. A. Balmaseda, S. Abdalla, E. Källén, and P. E. M. Janssen, 2014: How robust is the recent strengthening of the tropical Pacific trade winds? *Geophys. Res. Lett.*, **41**, 4398–4405, <https://doi.org/10.1002/2014GL060257>.
- Dee, D. P., and Coauthors, 2011: The ERA-Interim reanalysis: Configuration and performance of the data assimilation system. *Quart. J. Roy. Meteor. Soc.*, **137**, 553–597, <https://doi.org/10.1002/qj.828>.
- Deser, C., A. S. Phillips, and J. W. Hurrell, 2004: Pacific interdecadal climate variability: Linkages between the tropics and the North Pacific during boreal winter since 1900. *J. Climate*, **17**, 3109–3124, [https://doi.org/10.1175/1520-0442\(2004\)017<3109:PICVLB>2.0.CO;2](https://doi.org/10.1175/1520-0442(2004)017<3109:PICVLB>2.0.CO;2).
- , M. A. Alexander, S.-P. Xie, and A. S. Phillips, 2010: Sea surface temperature variability: Patterns and mechanisms. *Annu. Rev. Mar. Sci.*, **2**, 115–143, <https://doi.org/10.1146/annurev-marine-120408-151453>.
- Dewitte, B., and Coauthors, 2012: Change in El Niño flavours over 1958–2008: Implications for the long-term trend of the upwelling off Peru. *Deep-Sea Res. II*, **77–80**, 143–156, <https://doi.org/10.1016/j.dsr2.2012.04.011>.
- Dommenget, D., 2009: The ocean's role in continental climate variability and change. *J. Climate*, **22**, 4939–4952, <https://doi.org/10.1175/2009JCLI2778.1>.
- Dong, L., and M. J. McPhaden, 2016: Interhemispheric SST gradient trends in the Indian Ocean prior to and during the recent global warming hiatus. *J. Climate*, **29**, 9077–9095, <https://doi.org/10.1175/JCLI-D-16-0130.1>.
- Dufresne, J.-L., and Coauthors, 2013: Climate change projections using the IPSL-CM5 Earth system model: From CMIP3 to CMIP5. *Climate Dyn.*, **40**, 2123–2165, <https://doi.org/10.1007/s00382-012-1636-1>.
- England, M. H., and Coauthors, 2014: Recent intensification of wind-driven circulation in the Pacific and the ongoing warming hiatus. *Nat. Climate Change*, **4**, 222–227, <https://doi.org/10.1038/nclimate2106>.
- Falvey, M., and R. D. Garreaud, 2009: Regional cooling in a warming world: Recent temperature trends in the southeast Pacific and along the west coast of subtropical South America (1979–2006). *J. Geophys. Res.*, **114**, D04102, <https://doi.org/10.1029/2008JD010519>.
- Fichefet, T., and M. Maqueda, 1997: Sensitivity of a global sea ice model to the treatment of ice thermodynamics and dynamics.

- J. Geophys. Res.*, **102**, 12 609–12 646, <https://doi.org/10.1029/97JC00480>.
- Fleming, L. E., and K. J. Anchukaitis, 2016: North Pacific decadal variability in the CMIP5 last millennium simulations. *Climate Dyn.*, **47**, 3783–3801, <https://doi.org/10.1007/s00382-016-3041-7>.
- Folland, C., D. Parker, A. Colman, and R. Washington, 1999: Large scale modes of ocean surface temperature since the late nineteenth century. *Beyond El Niño: Decadal and Interdecadal Climate Variability*, A. Navarra, Ed., Springer Science & Business Media, 73–102.
- Forster, P. M., T. Andrews, P. Good, J. M. Gregory, L. S. Jackson, and M. Zelinka, 2013: Evaluating adjusted forcing and model spread for historical and future scenarios in the CMIP5 generation of climate models. *J. Geophys. Res. Atmos.*, **118**, 1139–1150, <https://doi.org/10.1002/JGRD.50174>.
- Foster, G., and S. Rahmstorf, 2011: Global temperature evolution 1979–2010. *Environ. Res. Lett.*, **6**, 044022, <https://doi.org/10.1088/1748-9326/6/4/044022>.
- Franchito, S. H., V. B. Rao, J. L. Stech, and J. A. Lorenzetti, 1998: The effect of coastal upwelling on the sea-breeze circulation at Cabo Frio, Brazil: A numerical experiment. *Ann. Geophys.*, **16**, 866–871, <https://doi.org/10.1007/S00585-998-0866-3>.
- Fréon, P., M. Barange, and J. Aristegui, 2009: Eastern boundary upwelling ecosystems: Integrative and comparative approaches. *Prog. Oceanogr.*, **83**, 1–14, <https://doi.org/10.1016/j.pocean.2009.08.001>.
- Garreaud, R., and R. Muñoz, 2005: The low-level jet off the west coast of South America: Structure and variability. *Mon. Wea. Rev.*, **133**, 2246–2261, <https://doi.org/10.1175/MWR2972.1>.
- , and M. Falvey, 2009: The coastal winds off western subtropical South America in future climate scenarios. *Int. J. Climatol.*, **29**, 543–554, <https://doi.org/10.1002/joc.1716>.
- Gastineau, G., H. Le Treut, and L. Li, 2008: Hadley circulation changes under global warming conditions indicated by coupled climate models. *Tellus*, **60A**, 863–884, <https://doi.org/10.1111/j.1600-0870.2008.00344.x>.
- , A. Friedman, M. Khodri, and J. Vialard, 2018: Global ocean heat content redistribution during the 1998–2012 Interdecadal Pacific Oscillation negative phase. *Climate Dyn.*, **53**, 1187–1208, <https://doi.org/10.1007/S00382-018-4387-9%20>.
- Grise, K. M., and Coauthors, 2019: Recent tropical expansion: Natural variability or forced response? *J. Climate*, **32**, 1551–1571, <https://doi.org/10.1175/JCLI-D-18-0444.1>.
- Gutiérrez, D., and Coauthors, 2011: Coastal cooling and increased productivity in the main upwelling zone off Peru since the mid-twentieth century. *Geophys. Res. Lett.*, **38**, L07603, <https://doi.org/10.1029/2010GL046324>.
- Held, I. M., and B. J. Soden, 2006: Robust responses of the hydrological cycle to global warming. *J. Climate*, **19**, 5686–5699, <https://doi.org/10.1175/JCLI3990.1>.
- Henley, B. J., J. Gergis, D. J. Karoly, S. Power, J. Kennedy, and C. K. Folland, 2015: A tripole index for the Interdecadal Pacific Oscillation. *Climate Dyn.*, **45**, 3077–3090, <https://doi.org/10.1007/s00382-015-2525-1>.
- Hourdin, F., and Coauthors, 2013: Impact of the LMDZ atmospheric grid configuration on the climate and sensitivity of the IPSL-CM5A coupled model. *Climate Dyn.*, **40**, 2167–2192, <https://doi.org/10.1007/s00382-012-1411-3>.
- Hu, Y., C. Zhou, and J. Liu, 2011: Observational evidence for poleward expansion of the Hadley circulation. *Adv. Atmos. Sci.*, **28**, 33–44, <https://doi.org/10.1007/s00376-010-0032-1>.
- , L. Tao, and J. Liu, 2013: Poleward expansion of the Hadley circulation in CMIP5 simulations. *Adv. Atmos. Sci.*, **30**, 790–795, <https://doi.org/10.1007/s00376-012-2187-4>.
- Huang, B., and Coauthors, 2015: Extended Reconstructed Sea Surface Temperature version 4 (ERSST.v4). Part I: Upgrades and intercomparisons. *J. Climate*, **28**, 911–930, <https://doi.org/10.1175/JCLI-D-14-00006.1>.
- Ibarra, A. A., C. Reid, and A. Thorpe, 2000: The political economy of marine fisheries development in Peru, Chile and Mexico. *J. Latin Amer. Stud.*, **32**, 503–527, <https://doi.org/10.1017/S0022216X00005824>.
- Johanson, C. M., and Q. Fu, 2009: Hadley cell widening: Model simulations versus observations. *J. Climate*, **22**, 2713–2725, <https://doi.org/10.1175/2008JCLI2620.1>.
- Joshi, M. M., J. M. Gregory, M. J. Webb, D. M. H. Sexton, and T. C. Johns, 2008: Mechanisms for the land/sea warming contrast exhibited by simulations of climate change. *Climate Dyn.*, **30**, 455–465, <https://doi.org/10.1007/s00382-007-0306-1>.
- Kalnay, E., and Coauthors, 1996: The NCEP/NCAR 40-Year Reanalysis Project. *Bull. Amer. Meteor. Soc.*, **77**, 437–471, [https://doi.org/10.1175/1520-0477\(1996\)077<0437:TNYRP>2.0.CO;2](https://doi.org/10.1175/1520-0477(1996)077<0437:TNYRP>2.0.CO;2).
- Kämpf, J., and P. Chapman, Eds., 2016: The Peruvian-Chilean coastal upwelling system. *Upwelling Systems of the World*, Springer, 161–194.
- Kim, Y. H., S. K. Min, S. W. Son, and J. Choi, 2017: Attribution of the local Hadley cell widening in the Southern Hemisphere. *Geophys. Res. Lett.*, **44**, 1015–1024, <https://doi.org/10.1002/2016GL072353>.
- Knutson, T., J. P. Kossin, C. Mears, J. Perlwitz, and M. F. Wehner, 2017: Detection and attribution of climate change. *Climate Science Special Report: Fourth National Climate Assessment*, D. J. Wuebbles et al., Eds., Vol. I, U.S. Global Change Research Program, 114–132.
- Kociuba, G., and S. B. Power, 2015: Inability of CMIP5 models to simulate recent strengthening of the Walker circulation: Implications for projections. *J. Climate*, **28**, 20–35, <https://doi.org/10.1175/JCLI-D-13-00752.1>.
- Kohonen, T., 1998: The self-organizing map. *Neurocomputing*, **21**, 1–6, [https://doi.org/10.1016/S0925-2312\(98\)00030-7](https://doi.org/10.1016/S0925-2312(98)00030-7).
- Kravtsov, S., 2017: Pronounced differences between observed and CMIP5-simulated multidecadal climate variability in the twentieth century. *Geophys. Res. Lett.*, **44**, 5749–5757, <https://doi.org/10.1002/2017GL074016>.
- Krinner, G., and Coauthors, 2005: A dynamic global vegetation model for studies of the coupled atmosphere-biosphere system. *Global Biogeochem. Cycles*, **19**, GB1015, <https://doi.org/10.1029/2003GB002199>.
- Lamont, T., M. García-Reyes, S. J. Bograd, C. D. van der Lingen, and W. J. Sydeman, 2018: Upwelling indices for comparative ecosystem studies: Variability in the Benguela upwelling system. *J. Mar. Syst.*, **188**, 3–16, <https://doi.org/10.1016/j.jmarsys.2017.05.007>.
- L’Heureux, M., S. Lee, and B. Lyon, 2013: Recent multidecadal strengthening of the Walker circulation across the tropical Pacific. *Nat. Climate Change*, **3**, 571–576, <https://doi.org/10.1038/nclimate1840>.
- Li, G., and S.-P. Xie, 2014: Tropical biases in CMIP5 multimodel ensemble: The excessive equatorial Pacific cold tongue and double ITCZ problems. *J. Climate*, **27**, 1765–1780, <https://doi.org/10.1175/JCLI-D-13-00337.1>.
- Li, X., S. P. Xie, S. T. Gille, and C. Yoo, 2016: Atlantic-induced pan-tropical climate change over the past three decades. *Nat. Climate Change*, **6**, 275–279, <https://doi.org/10.1038/nclimate2840>.
- Lu, J., and B. Zhao, 2012: The role of oceanic feedback in the climate response to doubling CO₂. *J. Climate*, **25**, 7544–7563, <https://doi.org/10.1175/JCLI-D-11-00712.1>.

- , G. A. Vecchi, and T. Reichler, 2007: Expansion of the Hadley cell under global warming. *Geophys. Res. Lett.*, **34**, L06805, <https://doi.org/10.1029/2006GL028443>%20.
- Madec, G., 2008: NEMO Ocean engine. Institut Pierre-Simon Laplace (IPSL), Note du Pole de Modélisation 27, 300 pp.
- McLandress, C., T. G. Shepherd, J. F. Scinocca, D. A. Plummer, M. Sigmund, A. I. Jonsson, and M. C. Reader, 2011: Separating the dynamical effects of climate change and ozone depletion. Part II: Southern Hemisphere troposphere. *J. Climate*, **24**, 1850–1868, <https://doi.org/10.1175/2010JCLI3958.1>.
- McPhaden, M. J., S. E. Zebiak, and M. H. Glantz, 2006: ENSO as an integrating concept in earth science. *Science*, **314**, 1740–1745, <https://doi.org/10.1126/science.1132588>.
- Min, S. K., and S. W. Son, 2013: Multimodel attribution of the Southern Hemisphere Hadley cell widening: Major role of ozone depletion. *J. Geophys. Res. Atmos.*, **118**, 3007–3015, <https://doi.org/10.1002/JGRD.50232>.
- Minobe, S., 1997: A 50–70 year climatic oscillation over the North Pacific and North America. *Geophys. Res. Lett.*, **24**, 683–686, <https://doi.org/10.1029/97GL00504>.
- , 1999: Resonance in bidecadal and pentadecadal climate oscillations over the North Pacific: Role in climatic regime shifts. *Geophys. Res. Lett.*, **26**, 855–858, <https://doi.org/10.1029/1999GL900119>.
- Mitas, C. M., and A. Clement, 2005: Has the Hadley cell been strengthening in recent decades? *Geophys. Res. Lett.*, **32**, L03809, <https://doi.org/10.1029/2004GL021765>.
- Montecinos, A., S. Purca, and O. Pizarro, 2003: Interannual-to-interdecadal sea surface temperature variability along the western coast of South America. *Geophys. Res. Lett.*, **30**, 1570, <https://doi.org/10.1029/2003GL017345>.
- , O. Leth, and O. Pizarro, 2007: Wind-driven interdecadal variability in the eastern tropical South Pacific. *J. Geophys. Res.*, **112**, C04019, <https://doi.org/10.1029/2006JC003571>.
- Montzka, S. A., and Coauthors, 2018: An unexpected and persistent increase in global emissions of ozone-depleting CFC-11. *Nature*, **557**, 413–417, <https://doi.org/10.1038/s41586-018-0106-2>.
- Muñoz, R. C., and R. Garreaud, 2005: Dynamics of the low-level jet off the west coast of subtropical South America. *Mon. Wea. Rev.*, **133**, 3661–3677, <https://doi.org/10.1175/MWR3074.1>.
- Newman, M., and Coauthors, 2016: The Pacific decadal oscillation, revisited. *J. Climate*, **29**, 4399–4427, <https://doi.org/10.1175/JCLI-D-15-0508.1>.
- Nguyen, H., A. Evans, C. Lucas I. Smith, and B. Timbal, 2013: The Hadley circulation in reanalyses: Climatology, variability, and change. *J. Climate*, **26**, 3357–3376, <https://doi.org/10.1175/JCLI-D-12-00224.1>.
- , C. Lucas, A. Evans, B. Timbal, and L. Hanson, 2015: Expansion of the Southern Hemisphere Hadley cell in response to greenhouse gas forcing. *J. Climate*, **28**, 8067–8077, <https://doi.org/10.1175/JCLI-D-15-0139.1>.
- Nidheesh, A., M. Lengaigne, J. Vialard, T. Izumo, A. Unnikrishnan, and C. Cassou, 2017: Influence of ENSO on the Pacific decadal oscillation in CMIP models. *Climate Dyn.*, **49**, 3309–3326, <https://doi.org/10.1007/s00382-016-3514-8>.
- Oyarzún, D., and C. M. Brierley, 2019: The future of coastal upwelling in the Humboldt current from model projections. *Climate Dyn.*, **52**, 599–615, <https://doi.org/10.1007/s00382-018-4158-7>.
- Pérez, F. F., and Coauthors, 2010: Plankton response to weakening of the Iberian coastal upwelling. *Global Change Biol.*, **16**, 1258–1267, <https://doi.org/10.1111/j.1365-2486.2009.02125.x>.
- Power, S., T. Casey, C. Folland, A. Colman, and V. Mehta, 1999: Interdecadal modulation of the impact of ENSO on Australia. *Climate Dyn.*, **15**, 319–324, <https://doi.org/10.1007/s003820050284>.
- Quan, X.-W., M. P. Hoerling, J. Perlwitz, H. F. Diaz, and T. Xu, 2014: How fast are the tropics expanding? *J. Climate*, **27**, 1999–2013, <https://doi.org/10.1175/JCLI-D-13-00287.1>.
- Quijano-Vargas, J. J., 2011: Simulación de la dinámica del viento superficial sobre la costa de Ica utilizando el modelo numérico de la atmósfera de mesoescala MM5. M.S. thesis in Engineering in Fluid Mechanics, Universidad Nacional Mayor de San Marcos, 172 pp., <https://repositorio.igp.gob.pe/handle/IGP/83>.
- Renault, L., C. Deutsch, J. C. McWilliams, H. Frenzel, J. H. Liang, and F. Colas, 2016: Partial decoupling of primary productivity from upwelling in the California Current system. *Nat. Geosci.*, **9**, 505–508, <https://doi.org/10.1038/ngeo2722>.
- Reynolds, R. W., N. A. Rayner, T. M. Smith, D. C. Stokes, and W. Wang, 2002: An improved in situ and satellite SST analysis for climate. *J. Climate*, **15**, 1609–1625, [https://doi.org/10.1175/1520-0442\(2002\)015<1609:AHSAS>2.0.CO;2](https://doi.org/10.1175/1520-0442(2002)015<1609:AHSAS>2.0.CO;2).
- Riahi, K., and Coauthors, 2011: RCP 8.5—A scenario of comparatively high greenhouse gas emissions. *Climate Change*, **109**, 33–57, <https://doi.org/10.1007/s10584-011-0149-y>.
- Rousseaux, C. S. G., R. J. Lowe, M. Feng, A. M. Waite, and P. A. Thompson, 2012: The role of the Leeuwin Current and mixed layer depth on the autumn phytoplankton bloom off Ningaloo Reef, Western Australia. *Cont. Shelf Res.*, **32**, 22–35, <https://doi.org/10.1016/j.csr.2011.10.010>.
- Rykaczewski, R. R., J. P. Dunne, W. J. Sydeman, M. García-Reyes, B. A. Black, and S. J. Bograd, 2015: Poleward displacement of coastal upwelling-favorable winds in the ocean's eastern boundary currents through the 21st century. *Geophys. Res. Lett.*, **42**, 6424–6431, <https://doi.org/10.1002/2015GL064694>.
- Seidel, D. J., and W. J. Randel, 2007: Recent widening of the tropical belt: Evidence from tropopause observations. *J. Geophys. Res.*, **112**, D20113, <https://doi.org/10.1029/2007JD008861>.
- Small, R. J., E. Curchitser, K. Hedstrom, B. Kauffman, and W. G. Large, 2015: The Benguela upwelling system: Quantifying the sensitivity to resolution and coastal wind representation in a global climate model. *J. Climate*, **28**, 9409–9432, <https://doi.org/10.1175/JCLI-D-15-0192.1>.
- Son, S. W., and Coauthors, 2010: Impact of stratospheric ozone on Southern Hemisphere circulation change: A multimodel assessment. *J. Geophys. Res.*, **115**, D00M07, <https://doi.org/10.1029/2010JD014271>.
- Staten, P. W., J. J. Rutz, T. Reichler, and J. Lu, 2012: Breaking down the tropospheric circulation response by forcing. *Climate Dyn.*, **39**, 2361–2375, <https://doi.org/10.1007/s00382-011-1267-y>.
- , J. Lu, K. M. Grise, S. M. Davis, and T. Birner, 2018: Re-examining tropical expansion. *Nat. Climate Change*, **8**, 768–775, <https://doi.org/10.1038/s41558-018-0246-2>.
- Stouffer, R., S. Manabe, and K. Bryan, 1989: Interhemispheric asymmetry in climate response to a gradual increase of atmospheric CO₂. *Nature*, **342**, 660–662, <https://doi.org/10.1038/342660a0>.
- Strub, P. T., J. Mesías, V. Montecino, J. Rutllant, and S. Salinas, 1998: Coastal ocean circulation off western South America Coastal Segment (6,E). *The Global Coastal Ocean: Regional Studies and Syntheses*, A. R. Robinson and K. H. Brink, Eds., *The Sea—Ideas and Observations on Progress in the Study of the Seas*, Vol. 11, John Wiley and Sons, 273–314.

- Sverdrup, H. U., 1938: On the process of upwelling. *J. Mar. Res.*, **1**, 155–164, <https://doi.org/10.1357/002224038806440638>.
- Szopa, S., and Coauthors, 2013: Aerosol and ozone changes as forcing for climate evolution between 1850 and 2100. *Climate Dyn.*, **40**, 2223–2250, <https://doi.org/10.1007/s00382-012-1408-y>.
- Taylor, K. E., R. J. Stouffer, and G. A. Meehl, 2012: An overview of CMIP5 and the experiment design. *Bull. Amer. Meteor. Soc.*, **93**, 485–498, <https://doi.org/10.1175/BAMS-D-11-00094.1>.
- Timmermann, A., S. McGregor, and F. Jin, 2010: Wind effects on past and future regional sea level trends in the southern Indo-Pacific. *J. Climate*, **23**, 4429–4437, <https://doi.org/10.1175/2010JCLI3519.1>.
- Vargas, G., S. Pantoja, J. A. Rutllant, C. B. Lange, and L. Ortlieb, 2007: Enhancement of coastal upwelling and interdecadal ENSO-like variability in the Peru–Chile current since late 19th century. *Geophys. Res. Lett.*, **34**, L13607, <https://doi.org/10.1029/2006GL028812>.
- Vecchi, G. A., and B. J. Soden, 2007: Effect of remote sea surface temperature change on tropical cyclone potential intensity. *Nature*, **450**, 1066–1070, <https://doi.org/10.1038/nature06423>.
- Vigneau, E., and E. M. Qannari, 2003: Clustering of variables around latent components. *Commun. Stat. Simul. Comput.*, **32**, 1131–1150, <https://doi.org/10.1081/SAC-120023882>.
- Vuille, M., E. Franquist, R. Garreaud, W. Lavado, and C. Bolívar Cáceres, 2015: Impact of the global warming hiatus on Andean temperature. *J. Geophys. Res. Atmos.*, **120**, 3745–3757, <https://doi.org/10.1002/2015JD023126>.
- Wang, D., T. C. Gouhier, B. A. Menge, and A. R. Ganguly, 2015: Intensification and spatial homogenization of coastal upwelling under climate change. *Nature*, **518**, 390–394, <https://doi.org/10.1038/nature14235>.
- Waugh, D. W., C. I. Garfinkel, and L. M. Polvani, 2015: Drivers of the recent tropical expansion in the Southern Hemisphere: Changing SSTs or ozone depletion? *J. Climate*, **28**, 6581–6586, <https://doi.org/10.1175/JCLI-D-15-0138.1>.
- Xie, S.-P., C. Deser, G. A. Vecchi, J. Ma, H. Teng, and A. T. Wittenberg, 2010: Global warming pattern formation: Sea surface temperature and rainfall. *J. Climate*, **23**, 966–986, <https://doi.org/10.1175/2009JCLI3329.1>.